Advanced Functional Materials

ADVANCED FUNCTIONAL MATERIALS
www.afm-journal.de

RESEARCH ARTICLE

Neuromodulator-Inspired Gate-Tunable Tetracene–Metal Oxide Phototransistor for Adaptive Optoelectronic Memory and Neuromorphic Computing

Ahasan Ullah[1] | Roshell Lamug[2] | Tasnim Sarker[1] | Xueqiao Zhang[1] | Andrew Ensinger[1] | Lizhong Chen[1] | Oksana Ostroverkhova[2] | Li-Jing Cheng[1]

[1]School of Electrical Engineering and Computer Science, Oregon State University, Corvallis, Oregon, USA | [2]Department of Physics, Oregon State University, Corvallis, Oregon, USA

Correspondence: Li-Jing Cheng (chengli@oregonstate.edu)

Received: 1 December 2025 | **Revised:** 29 April 2026 | **Accepted:** 11 May 2026

Keywords: IGZO | neuromorphic | memory | neuromodulatory | phototransistors | persistent-photogating | tetracene

ABSTRACT

We present a neuromodulator-inspired organic–inorganic hybrid phototransistor that enables programmable optoelectronic memory and synaptic plasticity via dual optical–electrical modulation. The device integrates a tetracene-based photoactive polymer blend with an indium gallium zinc oxide (IGZO) thin-film transistor, forming a type-II heterojunction where photogenerated electrons transfer to the IGZO channel while holes are stored in deep trap states within the organic layer. These trapped charges induce persistent photogating, modulating channel conductance analogous to synaptic potentiation. Trap-dynamics modeling reveals that deep traps govern long-term retention, whereas shallow traps allow rapid adaptation. Gate bias further reshapes the trapped-charge distribution and tunes trapping–detrapping kinetics, achieving programmable transitions between short-term plasticity and long-term memory. Negative gate bias reinforces conductance retention (dopamine-like potentiation), whereas positive bias accelerates relaxation (serotonin-like depression), enabling polarity-controlled switching between analog learning, long-term storage, and controlled forgetting. Operating below 5 $\mu W \cdot cm^{-2}$, the device supports weak-light imaging (0.5 $\mu W \cdot cm^{-2}$), memory retention beyond 5000 s, and spatiotemporal trajectory tracking via transient charge storage. A device-calibrated artificial neural network using differential synapse pairs achieves >90% MNIST classification accuracy with near-linear weight updates over hundreds of cycles. These results demonstrate an energy-efficient platform unifying sensing, memory, and computation for neuromodulator-inspired in-sensor neuromorphic processing.

1 | Introduction

Biological sensory and synaptic systems achieve efficient information processing by co-locating memory and computation in the same physical elements. Synapses in neural networks both integrate signal transduction with adaptive storage, enabling massively parallel and energy-efficient computation. This stands in sharp contrast to conventional von Neumann computing architectures, where physically separated memory and processing units require constant data transfer, creating a "memory wall" that limits speed and power efficiency [1–6]. By embedding computation and memory within synapses, the human brain performs parallel processing with extraordinary efficiency [7, 8], inspiring neuromorphic computing strategies that seek to reproduce this principle in hardware [9, 10].

A key feature of biological systems is their ability to regulate not only the strength but also the duration of synaptic responses

through neuromodulatory control. Neuromodulators such as dopamine, serotonin, acetylcholine, and norepinephrine modulate synaptic plasticity by gating induction, tuning retention, and adjusting recovery of synaptic efficacy [11–13]. Specifically, reward- and novelty-related stimuli trigger dopaminergic neurons to release dopamine, which reinforces active synapses through long-term potentiation (LTP) [14, 15]. Conversely, during satiation, stress, or information updating, serotonergic neurons from the raphe nuclei release serotonin, which promotes long-term depression (LTD) and forgetting [12, 16]. Together, these neuromodulators dynamically tune learning and memory by strengthening or weakening synaptic connections in response to behavioral context (Figure 1a). Biological neuromodulation typically operates over seconds to minutes (and up to hours), as it relies on diffusion, receptor binding, and intracellular biochemical signaling cascades. In this work, we focus on emulating the functional role of such modulatory control, namely the dynamic regulation of memory retention and forgetting, rather than reproducing these slower timescales, while leveraging faster, electronically tunable dynamics that are advantageous for neuromorphic hardware and real-time signal processing.

Optoelectronic synaptic transistors emulate these behaviors by integrating light sensing and memory within a single device, achieving in-sensor computation akin to a "brain on camera." [17–19] Using light as the presynaptic input allows analog weight updates, high bandwidth, and low crosstalk in arrays, enabling artificial retinas to preprocess optical data and perform pattern recognition without digitization [20, 21]. Unlike prior optoelectronic synapses limited to optical input and lacking control over memory duration, our hybrid phototransistor introduces a tunable electrical dimension via gate bias polarity. The device couples a photoactive organic layer, capable of storing long-lived trapped charges, with an oxide thin-film transistor (TFT) channel, where photoexcitation induces persistent photogating, enabling ultralow-power operation. While gate polarity programmably adjusts retention to reinforce or erase memory, analogous to biological neuromodulation. The synergy of strong photogating amplification and high trap density yields linear conductance modulation with pulse number and enables persistent conduction over a wide dynamic range, achieving adaptive, low-power neuromorphic operation unattainable in purely photo-driven devices.

In this device, optical excitation induces the accumulation of photogenerated trapped holes, forming the primary memory mechanism and mimicking dopaminergic reinforcement, where repeated activation strengthens synaptic efficacy through persistent potentiation. The gate voltage (V_g) additionally regulates this memory process in a polarity-dependent fashion by controlling the spatial distribution of trapped charges and, consequently, the photogating efficiency. As depicted in Figure 1b, a negative V_g deepens retention and consolidates the potentiated state, analogous to dopamine-driven synaptic strengthening during learning. In contrast, a positive V_g accelerating conductance decay, resembling serotonin-mediated depression and forgetting. This complementary photoelectrical control enables programmable transitions between potentiation and depression (Figure 1c), offering a hardware analog of the dopaminergic–serotonergic balance that dynamically regulates plasticity and memory persistence in biological neural systems.

Organic–inorganic hybrid phototransistors combine the strong light absorption and tunable trapping of organic semiconductors with the high mobility, stability, and low-noise transport of inorganic channels, overcoming the intrinsic limitations of purely organic devices. Organic semiconductors offer tunable optoelectronic properties and low-cost, solution-based fabrication [22, 23], but their low carrier mobility, typically one to two orders of magnitude lower than inorganics, necessitates high operating voltages and intense illumination [24–26]. For instance, threshold shifts of ∼50 V or illumination intensities of 5–20 mW·cm^{-2} are often required, and the corresponding pulse energies exceed the ∼10 fJ used per synaptic event in biology by a factor of 10^8 [25–32]. Moreover, their reliance on trap states for both charge storage and channel modulation limits conductivity and slows response [33].

These drawbacks are mitigated in hybrid architectures that pair a photoactive organic layer with an inorganic transport channel. In our design, the organic semiconductor 5,12-bis(triisopropylsilylethynyl)tetracene (TIPS-Tc) provides strong visible absorption and efficient exciton generation, long-lived excitons [34, 35], and deep hole traps that sustain conductance retention [36]. These properties lower the optical power threshold for synaptic modulation, enabling neuromorphic operation under weak illumination. The inorganic indium gallium zinc oxide (IGZO) channel contributes high carrier mobility, a wide bandgap, and stable carrier transport. At the type-II TIPS-Tc/IGZO heterojunction, excitons efficiently dissociate, transferring electrons to IGZO while holes are trapped in TIPS-Tc to yield persistent photogating crucial for synaptic and memory functions (Figure 1d). This hybrid design achieves sub −1 V gate operation, clear weight modulation at low optical fluxes near 1 μW·cm^{-2}, over two orders of magnitude lower than prior organic photosynaptic devices [26].

Although hybrid organic-oxide optoelectronic synapses have demonstrated promising functionalities, many operate under relatively high illumination, large bias, or limited electrical control. For example, a hybrid phototransistor synapse based on a donor–acceptor conjugated polymer/ITO interface [37] achieved optical bidirectional modulation under mW·cm^{-2}-level visible illumination and +10/−20 V bias, with responses approaching the noise floor at 0.096 mW·cm^{-2}. An IGZO/ZrAlO$_x$ synapse [38] demonstrated low-energy operation but relied on UV illumination (∼0.1 mW·cm^{-2}), while polyelectrolyte-gated organic synapses [39] required similar illumination levels. CsPbBr$_3$/ZnO perovskite/oxide arrays [40] further reduced detection thresholds but depend on two-terminal, intensity-driven switching without independent electrical tunability. In contrast, the present organic–oxide phototransistor operates at sub-μW·cm^{-2} visible light and enables gate-tunable photogating with potentiation, depression, and long-retention memory in a single device, offering clear advantages for low-light imaging and trajectory-tracking applications.

Beyond low-power operation, dual photo- and electro-gating provide versatile neuromorphic functionality. Weak gate bias produces short-term conductance changes, while stronger programming yields long retention lasting tens of minutes,

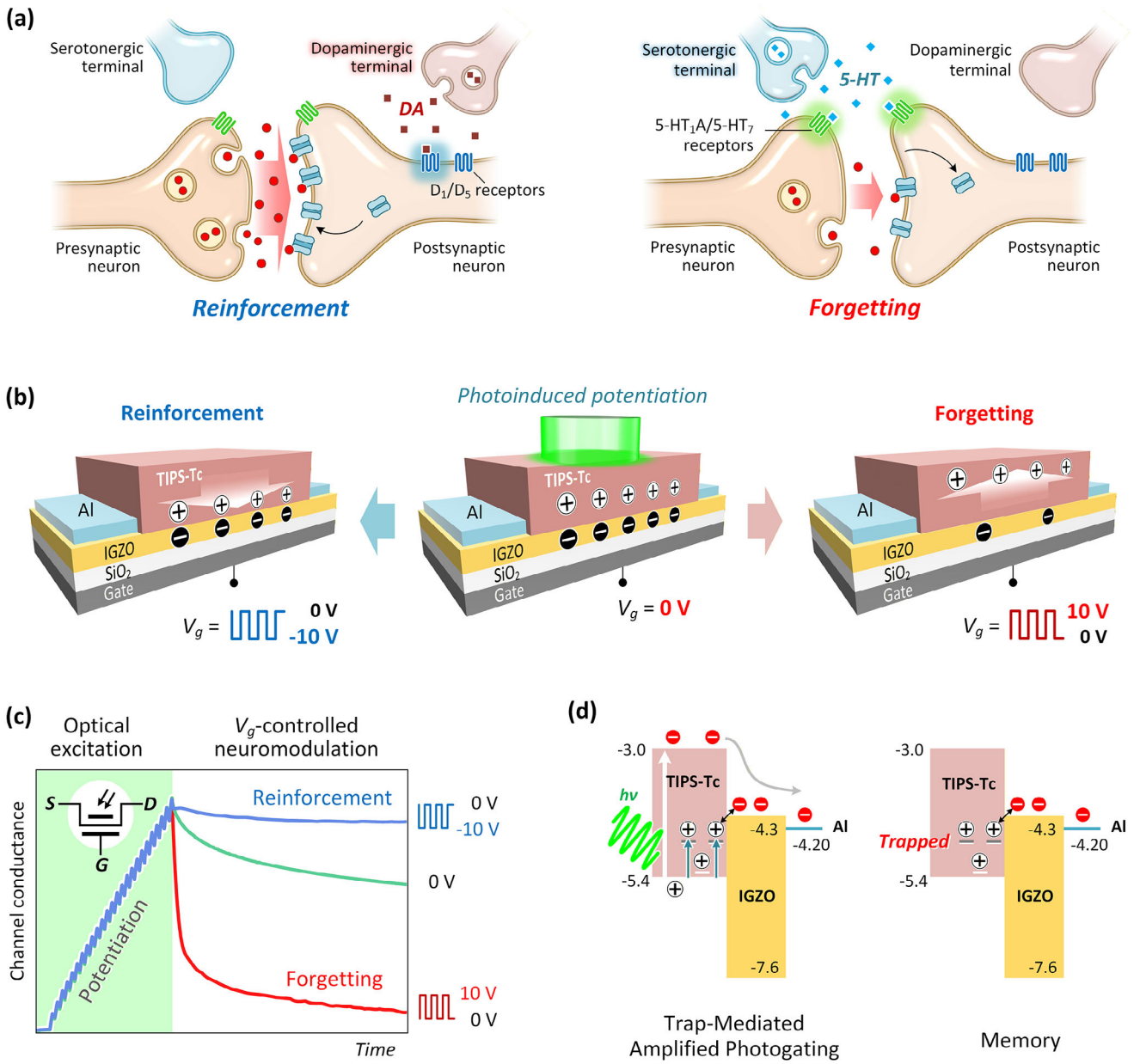

FIGURE 1 | (a) Schematic illustration of neuromodulator-regulated synaptic plasticity by dopamine and serotonin. The central synapse depicts communication between a presynaptic and postsynaptic neuron. Top: Dopaminergic neurons from the ventral tegmental area release dopamine (DA), which binds to D_1/D_5 receptors on the postsynaptic membrane, enhancing receptor insertion, strengthening transmission, and promoting long-term potentiation (LTP), underlying reinforcement and learning. Bottom: In contrast, serotonergic neurons from the raphe nuclei release serotonin (5-HT), which binds to 5-HT_1A receptors on pre- or postsynaptic sites, suppressing neurotransmitter release or promoting receptor internalization, leading to long-term depression (LTD) and forgetting. The complementary modulators dynamically tune synaptic strength, balancing memory retention and adaptive resetting. (b) Analogous neuromodulatory function in the hybrid TIPS-Tc/IGZO phototransistor: optical pulses induce trapped-hole accumulation and increase channel conductance via photogating (potentiation). Negative gate pulses preserve trapped charge, maintaining conductance (dopamine-like reinforcement or memory hold), while positive gate pulses accelerate detrapping for rapid recovery (serotonin-like reset or forgetting). (c) Channel conductance increases linearly during optical potentiation and exhibits gate-tunable relaxation after light-off. Inset: symbol of the synaptic phototransistor. (d) Band diagrams illustrating photogating: trapped holes near the heterojunction enhance transistor conductance and persist after light-off, sustaining memory behavior.

surpassing prior optoelectronic synapses. The device also offers linear, accumulative weight updates for accurate ANN training, unlike nonlinear memristive systems [9, 41–43]. Through coupled photoelectrical modulation, the TIPS-Tc/IGZO hybrid emulates dopamine-like reinforcement and serotonin-like depression, where optical excitation drives potentiation and gate polarity controls retention or depression. This biomimetic dual-modulation approach unifies sensing, memory, and computation within a single device, advancing compact and energy-efficient neuromorphic processing.

2 | Results and Discussion

2.1 | Design of the TIPS-Tc/IGZO Synaptic Phototransistor

The synaptic phototransistor comprises a heterojunction between TIPS-Tc blended with polymethylmethacrylate (PMMA) and an IGZO thin-film transistor (TFT) fabricated on a heavily doped silicon substrate with a 300 nm SiO_2 dielectric in a bottom-gate, top-contact configuration (Figure 1b). In this work, the blend composition is controlled such that the average intermolecular spacing between TIPS-Tc molecules is ~1 nm, mediated by the PMMA matrix. All device fabrication and material characterization are based on this TIPS-Tc:PMMA composite; for simplicity, we refer to it as "TIPS-Tc" throughout the paper unless otherwise specified. The device is fabricated on a heavily doped silicon substrate with a 300 nm SiO_2 dielectric in a bottom-gate, top-contact configuration (Figure 1b). The doped silicon serves as the gate electrode, and patterned aluminum source-drain contacts define a channel 100 μm long and 1000 μm wide. The IGZO layer exhibits a field-effect mobility exceeding 14 $cm^2V^{-1}s^{-1}$ and a subthreshold swing of 356 mV dec^{-1} (Figure S1), achieved through optimized O_2 partial pressure during sputtering followed by thermal annealing (see Experimental).

The band alignment between TIPS-Tc and IGZO forms a type-II heterojunction (Figure 1d) that facilitates efficient electron–hole separation. TIPS-Tc has HOMO/LUMO levels of −5.4 eV/−3.0 eV, while IGZO features a conduction band minimum at −4.30 eV and a valence band maximum at −7.60 eV, positioning TIPS-Tc as the electron donor and IGZO as the acceptor. In this architecture, TIPS-Tc serves dual functions. First, it strongly absorbs visible light to generate excitons that dissociate at the TIPS-Tc/IGZO interface. Second, it provides deep trap states that capture and retain photogenerated holes beyond illumination. These trapped holes establish a persistent internal electric field that sustains IGZO channel conductance, producing a long-lived photogating effect that persists after illumination and emulates synaptic memory.

The molecular structure of TIPS-Tc (Figure 2a) features an extended π-system compared with shorter acenes such as anthracene. As shown in Figure 2b, TIPS-Tc exhibits three excitonic absorption peaks at ~537, 500, and 465 nm, corresponding to the 0–0, 0–1, and 0–2 vibronic components of the $S_0 \rightarrow S_1$ π–π^* excitation in the tetracene core. The interpeak spacing (~1.4–1.5 $\times 10^3$ cm^{-1}) indicates coupling to high-frequency C═C stretching modes, concentrating oscillator strength in the green region. In contrast, IGZO is largely transparent in the visible range, ensuring minimal optical loss and efficient photon harvesting by the organic layer.

Photoluminescence (PL) measurements confirm efficient interfacial charge transfer. Transient PL (Figure 2c) shows that the average exciton lifetime of TIPS-Tc decreases from 4.5 ns (pristine film) to ~1.5 ns on IGZO, based on biexponential fits to time-correlated single-photon counting (TCSPC) data (Table S1). This reduction indicates an additional nonradiative decay pathway via charge transfer. Details of the fitting and lifetime analysis are provided in Section S1. Steady-state PL (Figure 2d) is also partially quenched for TIPS-Tc on IGZO, consistent with rapid exciton dissociation and charge transfer at the heterojunction.

Collectively, these structural, optical, and electrical characteristics establish that the TIPS-Tc/IGZO heterojunction supports strong visible absorption, favorable band alignment, and efficient charge transfer. The long-lived memory behavior observed later in this work likely originates from morphology- and oxygen-related deep traps in TIPS-Tc, providing the charge-retention mechanism essential for persistent photogating and synaptic function [44, 45].

2.2 | Electrical Characteristics of TIPS-Tc/IGZO Synaptic Phototransistor

Figure 3a compares transfer characteristics in the dark, under 535 nm illumination, and 60 s after light-off. Illumination induces a clear negative threshold-voltage (V_{th}) shift from 0.42 to −1.5 V (extracted via the second-derivative method) [46] and increases the off current (I_{off}) due to photoinduced electron transfer from TIPS-Tc to IGZO, which raises the channel electron density. While I_{off} fully recovers to its dark baseline, the V_{th} shift remains, indicating long-lived positive charges trapped in the TIPS-Tc/PMMA layer electrostatically bias the channel rather than defect generation or persistent photoconductivity in IGZO. If the latter were present, a sustained I_{off} increase or subthreshold swing change would occur after light-off, but neither is observed. Control measurements on a bare IGZO TFT (Figure S2) show no discernible V_{th} shift or I_{off} change under identical illumination, further confirming that the effect originates from photoinduced charge trapping in TIPS-Tc.

Figure 3b,c shows the output characteristics in the dark and under illumination, respectively. Light markedly enhances the drain current at fixed gate bias, with linear behavior up to V_{ds} ≈ 1 V. Hence, subsequent measurements were performed at V_{ds} = 1 V to ensure linear operation at V_g = −0.5 V. This condition is critical for neuromorphic operation, where channel conductance (G) encodes synaptic weight, and V_{ds} serves as the input. Operating in the Ohmic region ($I_{ds} = G \cdot V_{ds}$) ensures accurate multiply–accumulate computation, while operation in saturation introduces nonlinear I_{ds}–V_{ds} behavior, reducing dynamic range and increasing readout error and power consumption.

Synaptic phototransistors emulate biological synapses, where presynaptic spikes elicit excitatory postsynaptic currents (EPSCs), transient signals shaped by rapid neurotransmission and slower processes, such as receptor modulation and structural plasticity underlying long-term memory [47]. In the TIPS-Tc/IGZO device, an optical pulse serves as the presynaptic input: photoexcitation induces excess hole trapping in the TIPS-Tc:PMMA layer near the heterojunction, which electrostatically gates the channel and produces an EPSC-like transient in the drain current. Here, the postsynaptic response is represented by ΔEPSC, defined as the change in drain current relative to the dark current ($\Delta EPSC = I_{ds} - I_{dark}$). Under a single 535 nm pulse (5 μW·cm^{-2}, 10 s), the drain current rises rapidly by 16 nA (Figure 3d), then decays in two phases, with an initial fast drop followed by a slower relaxation to a residual ~5 nA. This biphasic decay reflects short- and long-term plasticity, with rapid detrapping corresponding to transient

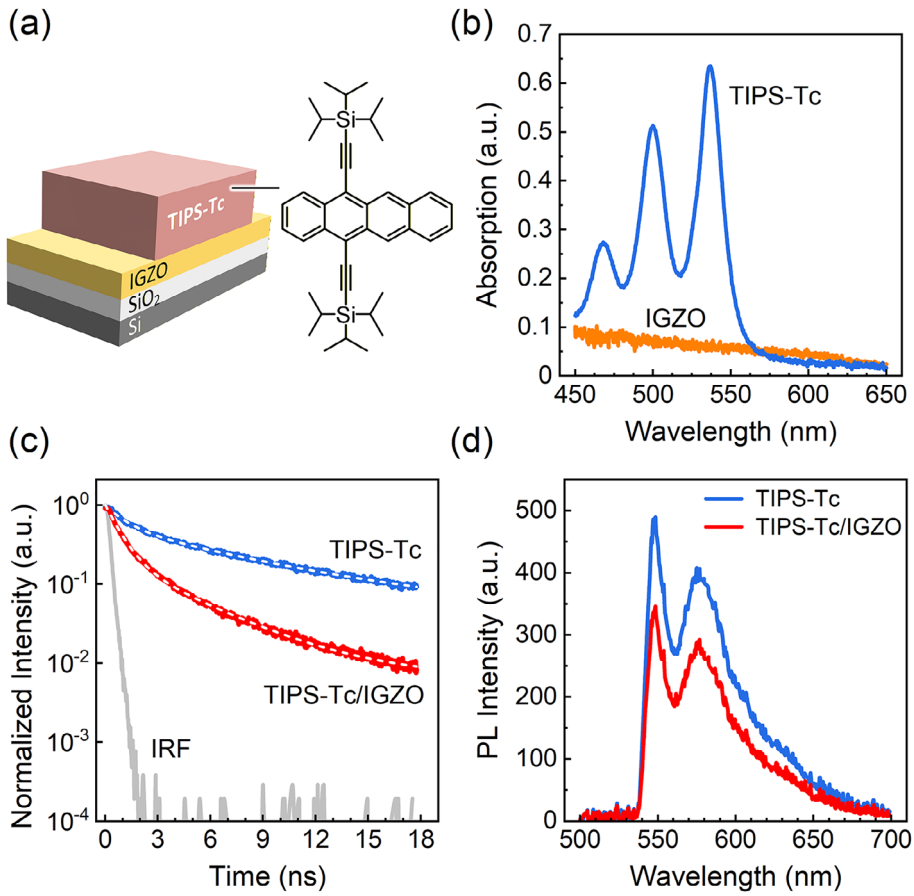

FIGURE 2 | (a) Device structure and TIPS-Tc molecular structure. (b) Absorption spectra of IGZO and TIPS-Tc thin films, revealing distinct excitonic peaks in TIPS-Tc and the optical transparency of IGZO across the visible range. (c) Transient photoluminescence (PL) decay curves for pristine TIPS-Tc and TIPS-Tc/IGZO films, indicating shortened exciton lifetime due to interfacial charge transfer. (d) Steady-state PL spectra showing reduced emission of TIPS-Tc on IGZO, confirming efficient exciton dissociation and interfacial charge transfer.

relaxation and persistent trapped charge sustaining long-term retention, demonstrating the TIPS-Tc/IGZO phototransistor's potential for neuromorphic applications.

Paired-pulse facilitation (PPF) characterizes the device's transient synaptic plasticity across multiple timescales (Figure 3e). When two identical optical pulses are applied sequentially, the second EPSC peak (A_2) exceeds the first (A_1) because holes trapped during the first pulse only partially detrap during the interpulse interval, leaving residual positive charges that accumulate and enhance photogating during the second pulse. The facilitation is quantified by the PPF index, defined as $(A_2/A_1) \times 100\%$.

Figure 3f shows the dependence of the PPF index on the inter-light-pulse interval (Δt) at $V_g = -0.5$, 0, and 0.5 V. As Δt increases from 0.2 to 32 s, the PPF index decays exponentially, resembling short-term memory fading in biological synapses. The strongest PPF occurs at $V_g = -0.5$ V, consistent with enhanced interfacial trap-charge retention under negative bias. As V_g becomes more positive, retention decreases, and the PPF correspondingly diminishes. Current traces at $V_g = -0.5$ V for PPF analysis are shown in Figure S3. The data fit well to a biexponential model,

$$PPF = A_1 e^{-\Delta t/\tau_1} + A_2 e^{-\Delta t/\tau_2} + C \quad (1)$$

where A_1, τ_1 and A_2, τ_2 represent the amplitudes and relaxation times of fast and slow components, respectively, and C is the long-term baseline. Excellent fits ($R^2 = 0.991$-0.997) yield $\tau_1 \approx 1.30$, 1.62, and 1.41 s, and $\tau_2 \approx 10.50$, 5.80, and 19.29 s for $V_g = -0.5$, 0, and 0.5 V, respectively (full parameters in Table S2). Notably, the much longer τ_2 values, roughly an order of magnitude longer than τ_1, reveal distinct fast and slow facilitation timescales analogous to those in biological synapses [33]. Because of its superior charge-retention behavior, $V_g = -0.5$ V was selected for all subsequent synaptic device measurements.

This dual-component behavior indicates that the device integrates information over two timescales: τ_1 governs the temporal bandwidth for rapid spike integration (< 1 s), while τ_2 extends short-term memory to ~10 s, enabling correlation of sparse events. The sustained PPF above 150% even at long intervals highlights deep-trap-assisted retention, providing a synaptic kernel capable of both fast event processing and temporally correlated tasks, such as motion detection and sequence recognition.

2.3 | Synaptic Weight Modulation and Plasticity

Synaptic plasticity is the adaptive strengthening or weakening of synaptic connections that underlie learning and memory.

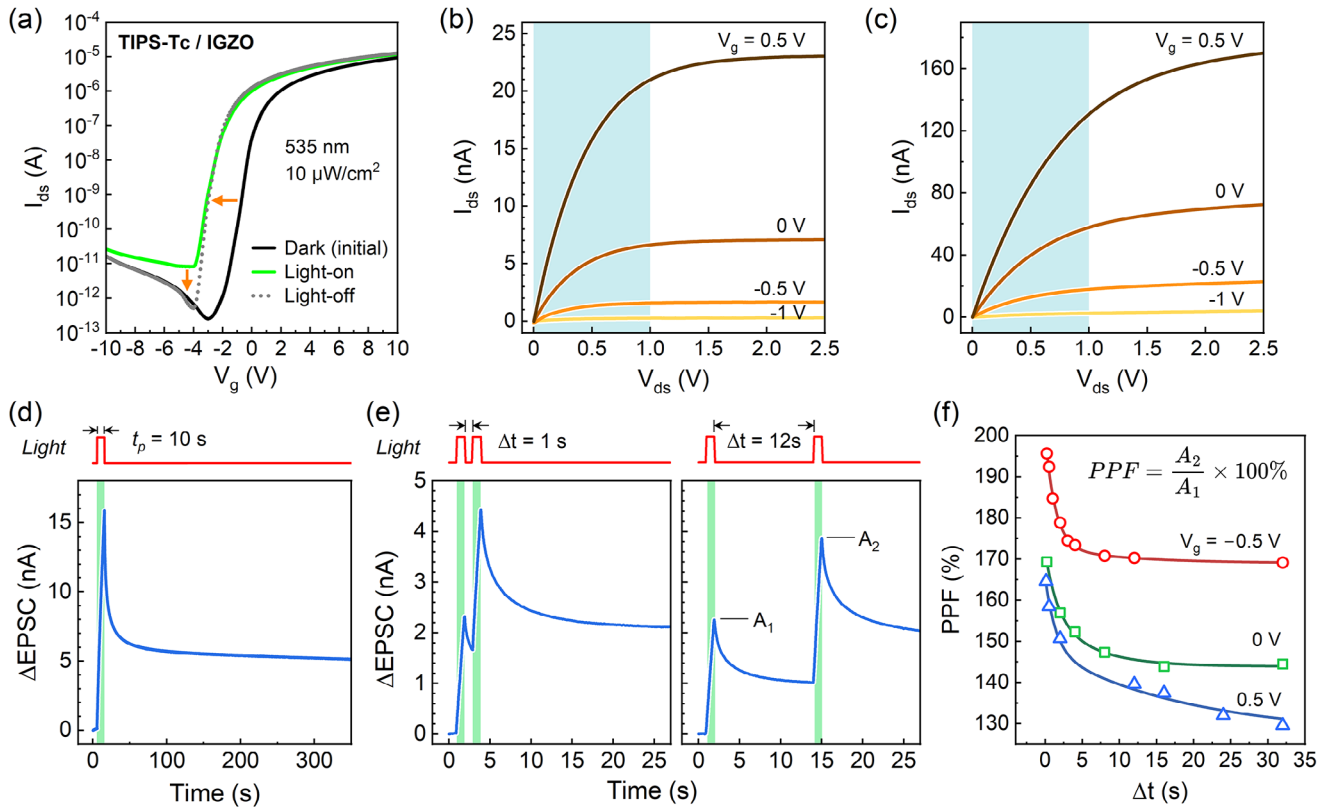

FIGURE 3 | (a) Transfer characteristics of the synaptic phototransistor under dark and illuminated conditions. (b) Output characteristics in the dark and (c) under illumination. Change in excitatory post-synaptic current (ΔEPSC) induced by (d) a single 10 s optical pulse (intensity: 5 μW·cm^{-2}) and (e) paired 1 s optical pulses with interpulse intervals (Δt) of 1 s and 12 s, measured at $V_g = -0.5$ V and $V_{ds} = 1$ V. (f) Paired-pulse facilitation (PPF) index as a function of Δt for three gate voltages, showing bias-dependent short-term plasticity. Solid lines show the model fits to experimental data based on Equation (1). All measurements were performed under 535 nm excitation; panels (a–c, e, f) used 10 μW· cm^{-2} illumination, and (d) used 5 μW·cm^{-2}.

This behavior is emulated in the TIPS-Tc/IGZO phototransistor through coordinated optical and electrical modulations. In this system, the drain current (I_{ds}) serves as the postsynaptic signal, modulated by photoinduced hole trapping in the TIPS-Tc/IGZO interface. Optical pulses act as presynaptic spikes that generate trapped holes, electrostatically gating the IGZO channel and potentiating I_{ds}, while V_g pulses induce synaptic depression by promoting charge redistribution and detrapping. Analogous to biological synapses, I_{ds} corresponds to the excitatory postsynaptic current, and the trapped holes represent slower regulatory processes that stabilize or adjust synaptic strength, enabling both short-term plasticity and long-term memory retention within a single device.

Figure 4 demonstrates optical and electrical control of synaptic behavior. Extending a single 535 nm optical pulse (5 μW·cm^{-2}) from 0.2 to 10 s raises the EPSC from 0.43 to 15.87 nA, with longer post-stimulus retention. The slow EPSC decay after light removal reflects persistent hole trapping in TIPS-Tc, signifying the emergence of long-term plasticity and stable memory retention within a single phototransistor. As shown in Figure 4b, increasing the number of 0.5 s pulses (5 μW·cm^{-2}) from 1 to 40 amplifies EPSC from 1.13 to 23.92 nA, revealing cumulative potentiation and indicating the transition from short-term potentiation (STP) to long-term potentiation (LTP). Figure 4c shows that EPSC scales linearly with optical power density (0.1–10 μW·cm^{-2}) under a fixed 10 s pulse, confirming light intensity as a reliable control for synaptic weight. Figure 4d examines the wavelength dependence (10 μW·cm^{-2}, 5 s, 450–650 nm); the EPSC spectrum follows the TIPS-Tc absorption (Figure 2b), confirming that the organic layer is the primary source of the response. Within 535–555 nm, the behavior remains nearly linear, enabling wavelength-tunable synaptic modulation.

Finally, Figure 4e validates V_g-dependent synaptic plasticity through channel conductance modulation. Optical potentiation (535 nm, 5 μW·cm^{-2}, 50 pulses, 1 s width, 2 s period) raises conductance to 43.8 nS. Subsequent electrical depression under two gate-bias conditions reveals distinct behaviors: positive V_g pulses (oscillating between 10 and −0.5 V, 1 s width, 2 s period) rapidly suppress the conductance by about 60% after a single pulse and subsequently decline to 5.7 nS after 50 pulses, while constant $V_g = -0.5$ V gradually lowers it to 29.0 nS. In addition, 14 consecutive potentiation-depression cycles were performed (Figure S4), demonstrating stable and repeatable conductance modulation without noticeable degradation, confirming reliable V_g-controlled synaptic operation.

2.4 | Operating Mechanism of TIPS-Tc/IGZO Synaptic Phototransistors

To investigate gate-dependent retention dynamics, Figure 5a presents $I_{ds}(t)$ measured under 535 nm illumination (1 μW·cm^{-2},

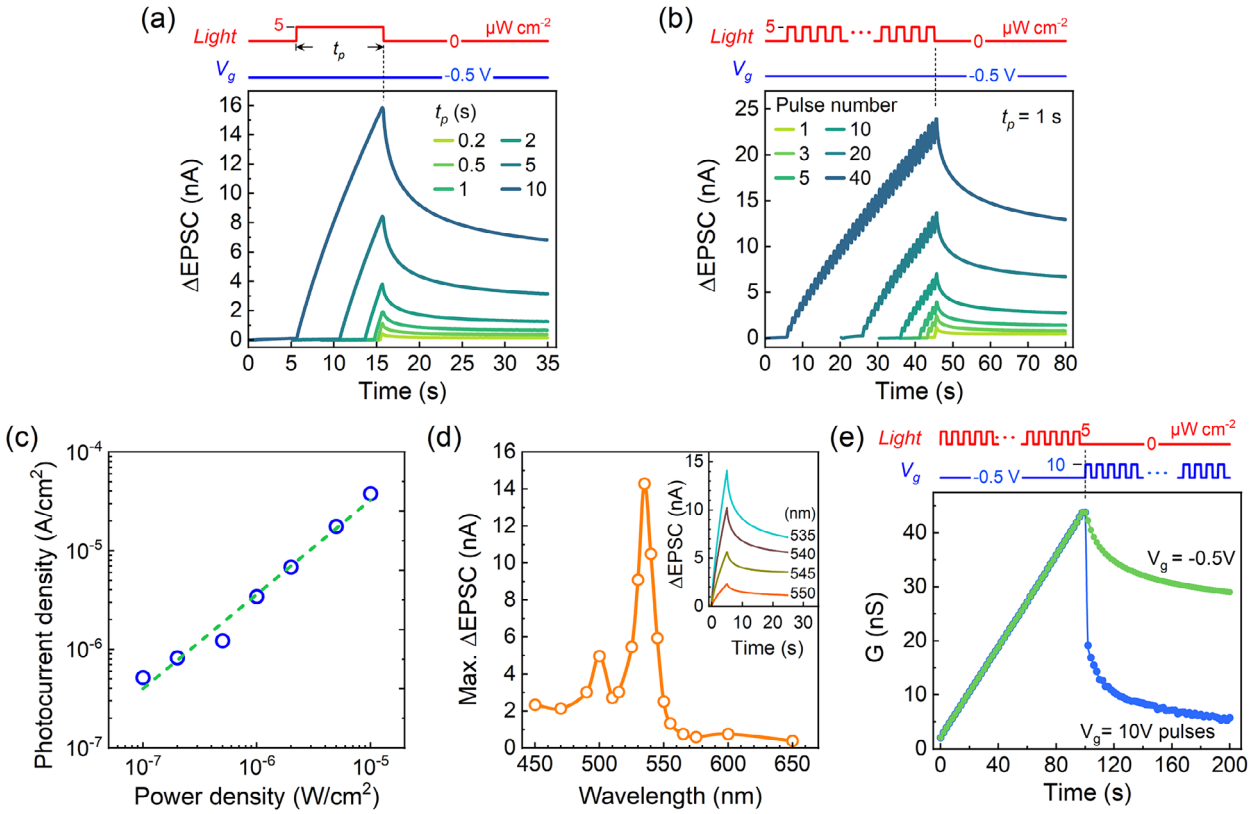

FIGURE 4 | Modulation of ΔEPSC measured at $V_{ds} = 1$ V, illustrating the transition from short-term potentiation (STP) to long-term potentiation (LTP) as a function of (a) single-pulse duration, (b) pulse number, (c) optical power density, and (d) excitation wavelength. (e) Synaptic plasticity via optical potentiation (LTP) followed by electrical depression (LTD) under positive V_g pulses (10–−0.5 V, 1 s width, 2 s period) and constant $V_g = -0.5$ V, showing distinct depression dynamics.

50 s) followed by 250 s relaxation at constant gate biases of $V_g = -0.5$, 0, and +0.5 V (timing diagram in inset). The gate bias primarily sets the overall current magnitude: positive V_g enhances channel conduction, yielding the largest I_{ds}. However, the current change relative to its initial dark baseline ($I_{ds}-I_{dark}$) reveals distinct photogating and memory behavior. Upon illumination, I_{ds} rises quasi-linearly over time as trapped holes accumulate, reinforcing the photogating field. The photocurrent changes reach ~16, 34, and 28 nA for $V_g = -0.5$, 0, and +0.5 V, respectively, with the maximum response at $V_g = 0$, reflecting a trade-off between gate-controlled channel conductance and photogating efficiency.

After light-off at $t = 50$ s, I_{ds} decays only partially over 250 s, with the fastest decay at positive V_g and the slowest at −0.5 V. A control IGZO TFT without TIPS-Tc (Figure S5) shows negligible photocurrent under identical conditions, confirming that retention originates from the TIPS-Tc layer rather than IGZO persistent photoconductivity. Furthermore, weak 535 nm excitation (≤ 5 μWcm^{-2}) cannot activate deep oxygen-vacancy states in IGZO, excluding their contribution. Notably, the slow I_{ds} decay far exceeds the nanosecond–microsecond recombination times typical of organic semiconductors, indicating long-lived trapped-charge behavior.

This retention arises from hole trapping in the heterojunction interface and within the bulk TIPS-Tc, which sustains an electrostatic photogate on the IGZO channel. In blended or polycrystalline TIPS-Tc:PMMA, traps can originate from structural disorder, grain boundaries, energetic tail states near the HOMO, and ambient-induced oxygen or water complexes. Additional trap states form at the TIPS-Tc/IGZO heterointerface due to structural and chemical discontinuities [48–50], producing multi-timescale trapping consistent with the observed decay [51].

The V_g-dependent trapped hole density Q(t) in the TIPS-Tc layer was extracted from the optically pulsed device structure depicted in Figure S6:

$$Q(t) = \frac{1}{\alpha}\left[\frac{C'_{ox}}{qd_{pg}}\left(\ln(10)\frac{kT}{q}\log\left(\frac{I_{ds}(t)}{n_0 K_{ch}}\right) - V_g\right) + \frac{d_{ch}}{d_{pg}}\frac{I_{ds}(t)}{K_{ch}}\right] \quad (2)$$

where C'_{ox} is the gate oxide capacitance per unit area, d_{pg} and d_{ch} are the thicknesses of the TIPS-Tc and IGZO layers, respectively, α is a V_g-dependent correction factor, n_0 is the equilibrium channel electron density, and K_{ch} is a prefactor determined by device geometry and material parameters [52].

Furthermore, Q(t) is modeled as the sum of shallow (T) and deep (M) trap populations: (Section S3).

$$Q(t) = T(t) + M(t) \quad (3a)$$

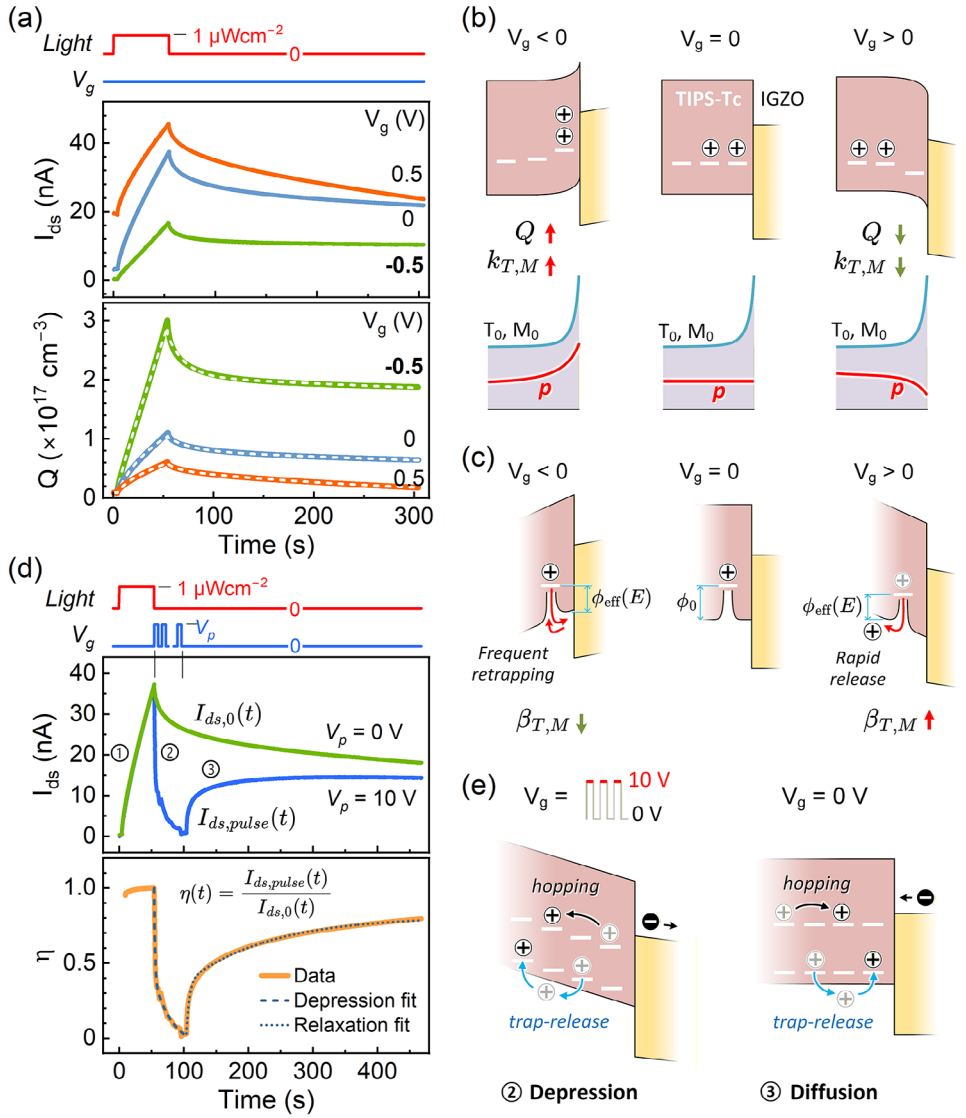

FIGURE 5 | Potentiation and depression mechanisms in TIPS-Tc/IGZO synaptic phototransistors. (a) V_g -dependent $I_{ds}(t)$ traces measured at V_{ds} = 1 V, showing potentiation and subsequent decay under a single optical pulse. Trapped-hole densities Q(t) in the TIPS-Tc layer, extracted at three constant gate biases, are fitted with a bi-exponential rise–decay model using Equation 3 (white dashed lines). (b) Band diagrams (top) and trap distributions (T_0, M_0) with V_g-controlled hole concentration profiles p in the TIPS-Tc layer (bottom), illustrating how gate polarity modulates spatial distribution of trapped holes and thereby affects total trapped-hole density Q and trapping rates $k_{T,M}$. (c) V_g -dependent band bending at the TIPS-Tc/IGZO interface governing hole retrapping (reduced $\beta_{T,M}$) or release (enhanced $\beta_{T,M}$). For $V_g > 0$, the TIPS-Tc-side barrier is lowered, enabling Poole–Frenkel field-assisted emission ($\Phi_{eff} < \Phi_0$); for $V_g < 0$, the TIPS-Tc/IGZO band offset suppresses release and stabilizes trapped carriers. (d) Comparison of depression dynamics under positive-gate pulsing and natural relaxation at $V_g = 0$ V. Optical potentiation (1) is followed by rapid conductance suppression (2) and partial recovery via hole diffusion (3), versus gradual decay without gate pulsing. Normalized charge-redistribution factor $\eta = I_{ds,pulse}/I_{ds,0}$ captures field-driven migration and diffusion-mediated redistribution during and after V_g pulsing, and is well described by a bi-exponential fit using Equation (S15). (e) Band diagrams illustrating field-driven hole redistribution during positive-gate pulsing and slower diffusion-mediated recovery after bias removal.

$$T(t) = \begin{cases} T_{ss} + (T_i - T_{ss})\, e^{-(k_T+\beta_T)t} & 0 \le t \le t_p \\ T(t_p)\, e^{-\beta_T(t-t_p)} & t > t_p \end{cases} \tag{3b}$$

$$M(t) = \begin{cases} M_{ss} + (M_i - M_{ss})\, e^{-(k_M+\beta_M)t} & 0 \le t \le t_p \\ M(t_p)\, e^{-\beta_M(t-t_p)} & t > t_p \end{cases} \tag{3c}$$

where k_T, k_M and β_T, β_M are the trapping and detrapping rates for shallow and deep states, respectively. In the present model, shallow and deep traps are treated as independent trap populations with distinct activation energies. This approximation captures the dominant retention dynamics using effective trapping and detrapping rates while maintaining a minimal set of kinetic parameters. Although carrier exchange or coupling between trap states may occur in practice, under the temporal resolution and bias conditions considered here, their net effect can be effectively incorporated into the averaged rate constants used in the model. This dual-trap approximation is well established in organic photorefractive materials, where shallow traps govern the response speed of erasable and rewriteable holograms, while deep traps support longer-term information storage. It has been widely successful in explaining experimental observations and guiding

TABLE 1 | Extracted parameters of the bi-exponential model.

V_g (V)	k_T (s^{-1})	k_M (s^{-1})	β_T (s^{-1})	β_M (s^{-1})	$T(t_p)$ (cm^{-3})	$M(t_p)$ (cm^{-3})	$Q(t_p)$ (cm^{-3})
−0.5	1.20×10^{-1}	1.80×10^{-3}	5.72×10^{-2}	3.86×10^{-4}	7.03×10^{16}	2.05×10^{17}	3.01×10^{17}
0	1.35×10^{-2}	3.50×10^{-4}	4.24×10^{-2}	9.07×10^{-4}	2.22×10^{16}	8.01×10^{16}	1.10×10^{17}
0.5	9.77×10^{-3}	2.70×10^{-4}	8.72×10^{-2}	3.88×10^{-3}	1.04×10^{16}	4.76×10^{16}	6.09×10^{16}

$T_0 = 1.04 \times 10^{17}$ cm^{-3}, $M_0 = 3.03 \times 10^{18}$ cm^{-3}

material design [53–55]. The steady-state trap occupancies are $T_{ss} = T_0\, k_T/(k_T + \beta_T)$ and $M_{ss} = M_0\, k_M/(k_M + \beta_M)$, with T_0, M_0 denoting the total densities of available shallow and deep traps. T_i and M_i are the initial occupancies of shallow and deep traps at the start of optical potentiation, which lasts $t_p = 50$ s.

The model fits the experimental I_{ds} data accurately across all gate biases (R^2 = 0.996–0.998), validating its use for quantitatively extracting the total trapped-hole density Q(t). Extracted parameters are summarized in Table 1. As shown in Figure 5a, Q(t) increases nearly linearly during the 50 s optical potentiation period for all three gate biases, with more negative V_g yielding larger Q. After light-off, Q decays biexponentially, featuring a fast initial component from shallow traps and a slower tail from deep traps. This multi-timescale decay accounts for the persistent photogating and memory-like retention behavior.

Analysis of Q(t) and its shallow T(t) and deep M(t) components at $t = t_p$ (the end of the potentiation period) shows that all decrease with increasing V_g, with deep traps dominating under all conditions ($M(t_p) > T(t_p)$). The larger M_0 compared to T_0 highlights that mid-gap traps are more abundant and energetically deeper than the shallow tail states. Interface disorder broadens the trap density of states (DOS) near the valence-band edge, forming shallow tail states that enable frequent trap-release cycles and yield a larger trapping rate k_T. In contrast, deep traps associated with impurities, oxidation products, grain boundaries, or ambient adsorbates retain carriers for extended periods, resulting in smaller k_M. In acene-based materials, photo-oxidation (e.g., quinone formation) and oxygen or moisture exposure further introduce deep traps, consistent with the large M_0 values reported previously for organic semiconductors [53].

The mechanism underlying the V_g-dependent trapped charge density Q is illustrated in Figure 5b. Under illumination, photogenerated electrons transfer from TIPS-Tc to IGZO, while holes are captured by trap states within the TIPS-Tc layer. These trapped holes act as an electrostatic photogate that enhances IGZO channel conductance and sustains elevated I_{ds} after light-off. The gate bias V_g not only directly modulates channel conductance but also controls the spatial distribution of holes within TIPS-Tc. Because Q depends on both the photogenerated hole density p and the spatial distribution of available trap states (T_0, M_0), and because trap density increases toward the TIPS-Tc/IGZO interface, the hole profile critically determines the effective trapped charge Q. Specifically, a negative V_g attracts holes toward the trap-rich TIPS-Tc/IGZO interface, increasing trap occupancy and strengthening photogating through stronger capacitive coupling to the channel, although the channel conductance itself is suppressed by the gate field. In contrast, a positive V_g pushes holes deeper into the TIPS-Tc bulk, where trap density is lower, thereby reducing the effective trapped charge contributing to photogating even though the channel conductance increases through the gate field effect.

The transient channel response, therefore, reflects the time evolution of the total trapped charge $Q(t)$, which arises from the combined contributions of shallow and deep trap populations as described in Equation (3a). Variations in $Q(t)$ shift the effective threshold voltage ($\Delta V_{th}(t) \propto Q(t)$), producing a drain current change $\Delta I_{ds}(t) \approx g_m \Delta V_{th}(t)$, where g_m is the channel transconductance. Consequently, the transient current response is proportional to the total trapped charge, with its dynamics directly tracking the evolution of the trapped charge population in TIPS-Tc.

The temporal behavior of this photogating response is governed by the different detrapping dynamics of shallow and deep traps. Shallow traps dominate the fast response component because holes captured in these states are released more readily and may recombine within the TIPS-Tc layer, leading to rapid photocurrent decay and partial irreversible charge loss. In contrast, deeper traps retain holes over longer timescales, sustaining the persistent photogating responsible for long-term synaptic memory.

The origin of trap states is closely linked to film morphology. By comparing the TIPS-Tc:PMMA film used in the main devices (average intermolecular TIPS-Tc spacing, d = 1 nm) with pristine TIPS-Tc, a more polymer-rich TIPS-Tc:PMMA film (d = 2 nm), and a dilute TIPS-Tc solution in toluene, photoluminescence measurements (Figure S7) show that all films remain predominantly amorphous, indicating the absence of long-range molecular ordering. Transient photocurrent (EPSC) measurements and model-extracted detrapping rates (β_T, β_M) (Figure S8) show that increasing PMMA content promotes deeper traps with reduced detrapping rates and enhanced long-term memory, whereas pristine films exhibit shallower traps and faster detrapping. These results suggest that shallow traps are associated with energetic disorder within TIPS-Tc aggregates, while deep traps originate from the TIPS-Tc:PMMA mixed morphology, where polymer-induced separation creates energetic and spatial barriers to detrapping; a detailed discussion is provided in Section S4 of the Supporting Information.

The gate bias also influences the trapping and detrapping kinetics. The trapping rates k_T and k_M decrease under more positive V_g as they scale with the local hole concentration p and the intrinsic capture coefficient γ ($k = \gamma p$, see Section S3). As depicted in Figure 5b, a negative V_g attracts photogenerated holes toward the trap-rich interface, increasing the local hole density and thereby enhancing the capture probability, resulting in larger k_T and k_M. On the contrary, a positive V_g redistributes holes into the TIPS-Tc bulk, reducing the interfacial hole population

and consequently suppressing trapping rates. This behavior is consistent with interfacial-trap–dominated photogating observed in other organic transistors [56, 57].

In contrast to trapping, the detrapping kinetics exhibit an opposite dependence on gate bias. As shown in Figure 5c, the detrapping rates β_T and β_M increase with more positive V_g. A positive gate bias drives holes away from the interface toward the TIPS-Tc bulk, aligning the electric field with the escape direction and facilitating release from trap states. Conversely, a negative V_g pulls holes toward the TIPS-Tc/IGZO interface, where the large valence-band offset suppresses hole emission across the heterojunction, resulting in slower detrapping. In addition, shallow traps respond more rapidly than deep traps due to their lower activation barriers ($\beta_T > \beta_M$), consistent with the observed fast and slow relaxation components. These trends explain the strong gate dependence of the extracted kinetic parameters and reinforce the role of interfacial trapping in governing the behavior of photogated transistors [4].

The gate-dependent detrapping behavior can be further understood within the framework of the Poole–Frenkel (PF) field-assisted emission model [58]. In this model, the applied electric field reduces the energy barrier for carrier emission from trap states (Figure 5c). Specifically, the barrier lowering under an electric field E is given by

$$\Delta\phi_{\mathrm{PF}}(E) = \sqrt{\frac{q^3 E}{\pi\epsilon}}$$

where q is the elementary charge and $\varepsilon = \varepsilon_0\,\varepsilon_r$ is the permittivity of the surrounding medium. The corresponding field-dependent detrapping rate is expressed as

$$\beta(E) = \nu_0 \exp\left[-\frac{\phi_{\mathrm{eff}}(E)}{k_B T}\right],\ \phi_{\mathrm{eff}}(E) = \phi_0 - \Delta\phi_{\mathrm{PF}}(E)$$

where $\phi_{\mathrm{eff}}(E)$ represents the effective emission barrier under an applied electric field, ϕ_0 is the zero-field activation energy for hole detrapping, k_B is the Boltzmann constant, and T is the temperature. The attempt-to-escape frequency ν_0 can be related to the trap capture coefficient via $\nu_0 = \gamma N_v$, where N_v is the effective density of states in the valence band.

Both trapping and detrapping processes also exhibit temperature dependence through the trap capture coefficient γ. The capture coefficient is generally expressed as $\gamma = v_{th}\,\sigma$, where v_{th} is the carrier thermal velocity, and σ is the capture cross-section. However, in disordered organic semiconductors such as TIPS-Tc, where charge transport is dominated by thermally activated hopping, the capture process is more accurately governed by carrier mobility μ rather than by v_{th} alone. In this regime, γ effectively inherits the temperature dependence of μ, which exhibits a much stronger temperature dependence than the conventional thermal velocity scaling $v_{th} \propto \sqrt{T}$ [59]. Depending on the underlying energetic disorder landscape, this behavior is typically described by either an Arrhenius-type relation $\mu \propto \exp(-E_a/k_B T)$ or a Gaussian disorder model $\mu \propto \exp[-(T_0/T)^2]$, where E_a is the activation energy associated with hopping transport and T_0 is a characteristic temperature reflecting the degree of energetic disorder [59]. This distinction becomes particularly important when considering temperature-dependent trapping and detrapping dynamics.

As a result, both trapping and detrapping rates inherit this stronger temperature dependence through γ, while the exponential dependence in the PF model further amplifies the temperature effect on detrapping. Consequently, increasing temperature accelerates the release of trapped holes and shortens retention time, whereas lower temperatures suppress hopping transport and thermally activated emission, stabilizing the trapped charge populations.

Temperature-dependent electrical measurements will provide valuable insight into trap activation energies and attempt-to-escape frequencies, and are part of our planned future investigations. In the present work, we focus on isolating gate-field-dependent trapping dynamics under well-controlled, fixed conditions to establish a clear physical framework. Within this context, the PF framework provides a physically grounded basis for understanding the temperature effect on retention behavior.

In this model, two distinct trap populations are considered: shallow traps (T) and deeper traps (M), characterized by different activation energies ϕ_T and ϕ_M ($\phi_T < \phi_M$). Their corresponding detrapping rates can therefore be expressed as

$$\beta_T(E) = \beta_{T0} \exp\left(\frac{\Delta\phi_{\mathrm{PF}}(E)}{k_B T}\right), \beta_M(E) = \beta_{M0} \exp\left(\frac{\Delta\phi_{\mathrm{PF}}(E)}{k_B T}\right)$$

where $\beta_{T0} = \nu_0 \exp(-\phi_T/k_B T)$ and $\beta_{M0} = \nu_0 \exp(-\phi_M/k_B T)$ represent the zero-field detrapping rates for shallow and deep traps, respectively.

These relations provide a physical interpretation of the experimentally extracted detrapping rates summarized in Table 1. Increasing V_g enhances the vertical electric field near the heterojunction, reduces the effective detrapping barrier, and increases both β_T and β_M. Due to the exponential dependence on barrier height, even modest field-induced barrier lowering can lead to substantial increases in detrapping rates. Under positive gate bias, the electric field lowers the barrier on the bulk side of the trap potential, thereby facilitating hole emission toward the TIPS-Tc bulk and leading to pronounced increases in both shallow and deep trap detrapping. In contrast, the weaker response under negative V_g arises from the band-alignment constraint at the TIPS-Tc/IGZO interface, which limits hole emission across the heterojunction.

To elucidate gate-controlled hole migration in TIPS-Tc, Figure 5d compares two depression conditions following identical optical potentiation (535 nm, 50 s): (i) constant $V_g = 0$ V as a control and (ii) a pulsed V_g waveform (0–10 V, 50% duty cycle, 2 s period) applied from $t = 50$ to 100 s during which the drain current $I_{ds,pulse}$ was recorded at the 0 V intervals. Under constant V_g, the drain current at zero gate bias ($I_{ds,0}$) decays gradually as holes relax from deep traps. In contrast, pulsed V_g causes a sharp drop in $I_{d,pulse}$, indicating field-driven hole migration away from the interface and suppressed photogating. When the pulsing stops (t > 100 s)

and V_g returns to 0 V, $I_{ds,pulse}$ partially recovers as holes diffuse back toward the interface.

The redistribution is quantified by a normalized charge-redistribution factor, $\eta(t) = I_{ds,pulse}(t)/I_{ds,0}(t)$, where $\eta = 1$ represents a trapped-charge distribution identical to that under $V_g = 0$ V, and smaller η values correspond to outward hole migration and reduced interfacial trapping. During potentiation, η stays near unity, whereas under pulsed-gate depression, η rapidly drops toward zero and, after pulse removal, quickly rebounds and partially recovers to ~0.8, reflecting field-driven hole migration followed by diffusion-mediated redistribution. A bi-exponential fit of $\eta(t)$ (Equation S15) resolves the fast and slow components, with the corresponding fitted parameters summarized in Table S3 (Section S5).

The analysis confirms that pulsed depression and subsequent relaxation are governed by distinct processes with different timescales. During depression, a fast decay dominates, consistent with field-driven release of interfacial traps that displace holes away from the TIPS-Tc/IGZO interface under strong positive V_g. During the following relaxation phase, hole transport is instead governed by slow, diffusion-mediated hopping among deeper traps with higher energy barriers, giving rise to the long redistribution tail. The incomplete recovery ($\eta < 1$) results from partial irreversible charge loss through field-assisted detrapping from shallow states and nonradiative recombination, whereas deep traps with weak field coupling remain occupied, sustaining residual photogating.

Figure 5e illustrates this mechanism. Under strongly pulsed positive V_g (+10 V), the electric field drives trapped holes away from the interface through two concurrent pathways [60]: (i) repeated trap-release among shallow states near the HOMO, where holes are thermally emitted and frequently re-trapped, and (ii) slow, thermally activated hopping among deeper localized states, due to higher energy barriers and weaker wavefunction overlap. Together, these processes shift the trapped-charge centroid farther from the IGZO channel, weakening capacitive coupling and causing rapid drain current suppression. When V_g is reset to 0 V, holes gradually diffuse back toward the interfacial traps, restoring photogating and partially recovering I_{ds}. Overall, rapid depression primarily arises from field-driven trap release at the interface, whereas slow diffusion-mediated retrapping at the interface yields only partial recovery, with irreversible loss originating from shallow-trap detrapping and recombination. This field-driven redistribution, followed by diffusion-mediated relaxation, agrees with interfacial-trap photogating models in thin-film and 2D semiconductors, where the spatial separation between trapped charge and the channel dictates both magnitude and timescale of persistent photoconductivity [61].

The large extracted deep-trap density ($M_0 \sim 10^{18}$ cm^{-3}) provides substantial trap capacity for charge redistribution, which supports stable gate-controlled conductance modulation within the operating range explored here. Under more extreme persistent-photocurrent conditions, progressive filling of deep traps could eventually limit the availability of additional trap states for redistribution, potentially reducing the precision of V_g-controlled conductance tuning.

2.5 | In-Sensor Memory–Enabled Applications

2.5.1 | Weak-Light Detection

In-sensor memory provides a unique advantage for detecting ultralow-power optical signals by enabling charge accumulation and temporal integration directly at the pixel level. Figure 6(a) demonstrates this capability in a 4 × 4 TIPS-Tc/IGZO synaptic phototransistor array under weak illumination (0.5 μW·cm^{-2}). In conventional CMOS imagers, achieving comparable weak-light capture requires long exposures, high gain, or multi-frame accumulation in external circuits and memory, all of which increase system complexity and power consumption [62, 63]. In contrast, the synaptic phototransistor inherently integrates optical flux over time, producing an output proportional to both light intensity and exposure duration without external circuitry.

To demonstrate array-level functionality, an "L"-shaped optical pattern was reconstructed on a 4 × 4 virtual array using temporal responses from independently characterized TIPS-Tc/IGZO phototransistors under 535 nm illumination at $V_g = -0.5$ V. Two operation modes were compared: (1) a single 1 s optical pulse as a non-integrating control (Figure 6b), functioning as a conventional photosensor, and (2) a train of 50 optical pulses (1 s width, 2 s period) for cumulative integration (Figure 6c). For each mode, intensity maps were generated from the peak I_{ds} at t = 0 s, immediately after one pulse or the 50-pulse sequence, and again after $t = 60$ s to evaluate retention. Dark pixels were derived from 60 s dark-current traces to correct for drift and variation. Corresponding $I_{ds}(t)$ transients are shown in Figure S9. Image contrast was quantified as:

$$C_a = \frac{I_p - I_d}{I_p + I_d},\ 0 \le C_a \le 1 \tag{4}$$

where I_p and I_d are the average currents of illuminated and dark pixels, respectively. For the single-pulse case, the "L" pattern was barely visible at $t = 0$ s ($C_a = 0.05$) and indistinguishable at $t = 60$ s ($C_a = 0.01$). In contrast, after 50 pulses, the "L" appeared clearly at $t = 0$ s ($C_a = 0.80$) and remained distinct at $t = 60$ s ($C_a = 0.75$). These results highlight that the synaptic array not only detects weak illumination but also retains the image via its intrinsic in-sensor memory, enabling high-contrast, low-light imaging without external accumulation or added circuitry.

To evaluate array-level reliability, pixel uniformity and inter-pixel crosstalk were characterized. Uniformity was assessed from transfer characteristics measured under dark conditions (Figure S10a), which show consistent operation across the array. The subthreshold swing and threshold voltage show moderate variation (Figure S10), with mean values of 418.9 mV/dec and 3.39 V with standard deviations of 167.5 mV/dec and 0.38 V, respectively. Despite this variation, its impact can be mitigated through pixel-wise calibration and normalization, enabling reliable operation for sensing tasks where relative signal modulation dominates. The variations are mainly attributed to nonuniformities in the organic layer and interfacial properties and can be further reduced through improved film deposition and interface engineering.

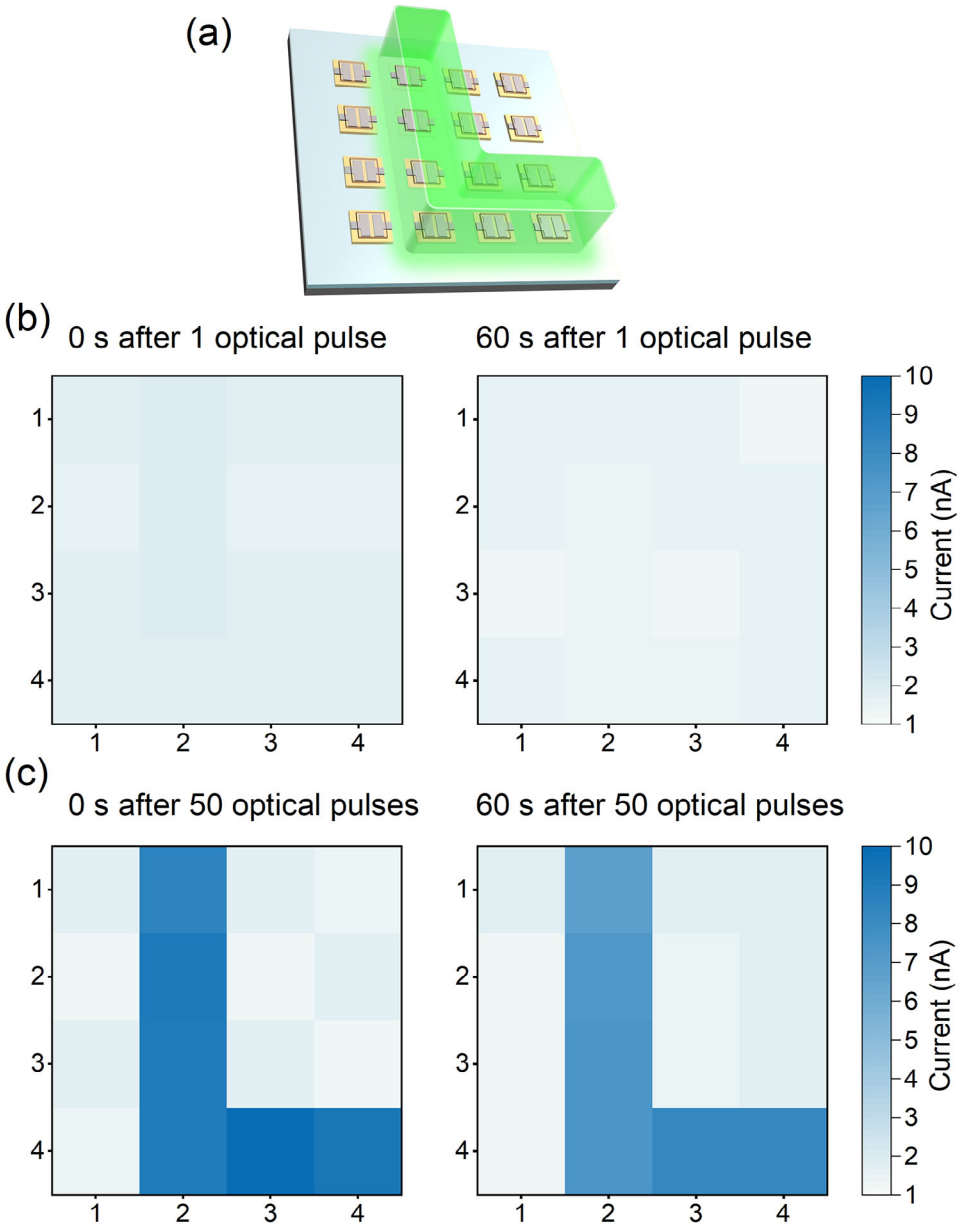

FIGURE 6 | (a) Weak-light detection in a synaptic phototransistor array via in-sensor, memory-assisted image retention. An "L"-shaped optical pattern is reconstructed onto a 4×4 array, where each pixel is a TIPS-Tc/IGZO synaptic phototransistor. (b) Response to a single 1 s, 535 nm optical pulse at 0.5 $\mu W \cdot cm^{-2}$, recorded immediately after illumination (0 s) and after 60 s. (c) Response to a train of 50 pulses (1 s width, 2 s period) under the same wavelength and intensity, recorded immediately after the final pulse and after 60 s. For all conditions, $V_g = -0.5$ V and $V_{ds} = 1$ V.

Crosstalk was assessed by monitoring non-illuminated pixels during pulsed optical stimulation of a selected device. As shown in Figure S11, adjacent and next-nearest pixels exhibit no photo response and negligible current variation, confirming effective suppression of both optical and electrical crosstalk. These results support the robustness of the array for spatially resolved sensing applications. Additionally, the signal-to-noise ratio (SNR) of the synaptic response to a single 0.25 s weak optical pulse (0.5 $\mu W \cdot cm^{-2}$) was evaluated. Using an RMS noise current of 4.8 pA extracted from the dark current response and a signal of ~0.4 nA in response to the optical pulse (Figure S9a), the SNR is calculated to be 38.4 dB, indicating strong signal integrity. This confirms that the response at 0.5 $\mu W \cdot cm^{-2}$ is clearly distinguishable from the noise floor.

2.5.2 | Optoelectronic Memory and Beam Trajectory Tracking

The synaptic phototransistor supports two modes controlled by gate bias. Under a near-zero V_g (subthreshold), it exhibits synaptic behavior with short-term memory, whereas large negative gate pulses enable long-term retention of photoinduced conductance, functioning as an optoelectronic memory. To demonstrate this mode, a "7"-shaped image was written onto a 4 × 4 array of independently measured TIPS-Tc/IGZO phototransistors driven by periodic negative gate pulses. Illuminated pixels received 25 optical pulses (535 nm, 5 $\mu W \cdot cm^{-2}$, 1 s width), while dark pixels served as references. Immediately after optical writing, all pixels were subjected to periodic V_g pulses (0 to −10 V, 1 s width, 2 s

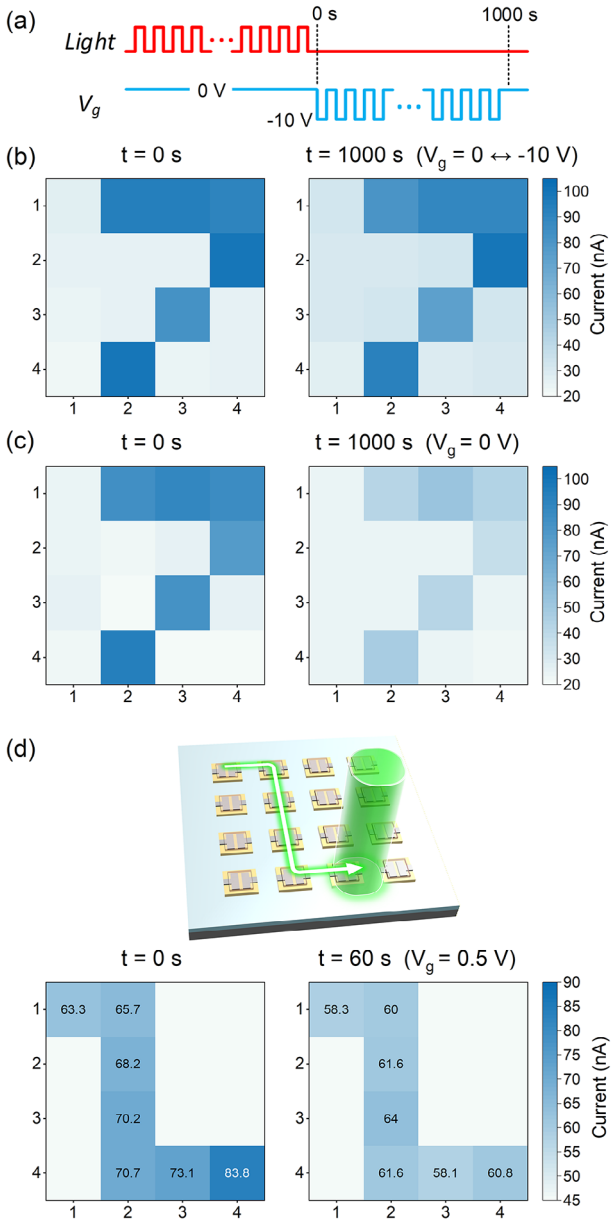

FIGURE 7 | Optoelectronic memory and beam-trajectory tracking in TIPS-Tc/IGZO synaptic phototransistors. (a–c) Optoelectronic memory: A "7"-shaped optical pattern was written onto a 4 × 4 array using 25 pulses (535 nm, 5 μW cm^{-2}, 1 s duration), with responses recorded at t = 0 s and t = 1000 s. (a) Optical and gate voltage V_g pulse timing diagrams. Readout performed under (b) periodically pulsed V_g between 0 and -10 V and (c) constant V_g = 0 V. (d) Beam-trajectory tracking: A scanning light beam moving from the top-left to bottom-right generated response maps at t = 0 s (immediately after leaving the last pixel) and t = 60 s, revealing gradient-based directionality and memory-induced persistence. Beam-trajectory tracking was conducted at V_g = 0.5 V to accelerate decay and enhance contrast. All devices were measured at V_{ds} = 1 V.

period) to sustain conductance (Figure 7a). The raw I_{ds} transients are shown in Figure S12, and extended retention up to 5000 s is presented in Figure S13.

Figure 7b,c compares array snapshots acquired immediately after writing (t = 0 s) and after 1000 s. With gate pulsing (Figure 7b), the mean current of illuminated pixels decreased slightly from 92.3 to 86.4 nA (~93% retention), whereas the control array without gate pulsing (V_g = 0 V, Figure 7c) decays from 89.2 to 45.7 nA (~51% retention). Image contrast (C_a, Equation (4)) showed a similar trend: decreasing modestly from 0.57 to 0.47 with pulsing, but sharply from 0.56 to 0.30 without. The slight contrast reduction observed with pulsed gate is partly attributable to a slight increase in dark-pixel current during retention (Figure S12d).

The retention mechanism under negative gate pulses aligns with the device operation principle described in Section 2.4. A sufficiently negative V_g drives trapped holes in bulk TIPS-Tc toward the TIPS-Tc/IGZO interface through hopping and trap-release processes, replenishing emptied interfacial sites that modulate IGZO channel conductance. Simultaneously, the negative bias suppresses interfacial detrapping, stabilizing the conductive state. This process resembles DRAM refreshing, with the bulk TIPS-Tc acting as a hole reservoir that periodically refills interfacial traps under negative gate pulses. A gate-pulse amplitude of −10 V was selected to balance interfacial hole supply and detrapping; more negative biases risk oversupplying migrated holes, leading to excessive channel conductance, while weaker ones fail to maintain conductance. Importantly, because the device remains off under large negative V_g during the refresh process, each cycle consumes minimal energy (~10 nW per pulse), demonstrating the energy efficiency of this optoelectronic memory.

Beyond static retention, the device's transient memory enables dynamic visual sensing, exemplified by optical beam tracking. Figure 7d illustrates beam-trajectory tracking using a reconstructed 4 × 4 array of independently measured devices. In this demonstration, a narrow 535 nm optical beam (5 μW·cm^{-2}) followed a step-shaped path intersecting seven pixels over 14 s, with each pixel exposed for 2 s. Sequential illumination produced a spatial gradient in retained current, with earlier pixels exhibiting conductance decay while later ones remained more conductive. Applying V_g = 0.5 V after illumination accelerated decay and enhanced contrast, allowing the motion direction to be directly inferred from current distribution: earlier pixels exhibited lower currents, while later ones exhibited higher. In the reconstructed array, the top-left pixel showed the lowest current and the bottom-right the highest, clearly revealing the direction of beam movement. The array's current snapshots, captured immediately after the beam finished its scan and left the last pixel (t = 0 s) and at 60 s (Figure 7d), visualize this gradient and its gradual fading. This behavior confirms in-sensor memory and demonstrates the capability to encode motion through transient photocurrent gradients. Temporal current traces for a 2 s photoexposure followed by 60 s retention for the devices are provided in Figure S14. Although 535 nm yielded the strongest response, wavelengths from 450–550 nm also yielded detectable signals consistent with the spectrum in Figure 4d.

2.5.3 | Artificial Neural Networks

To assess the neuromorphic computing potential of the synaptic phototransistor, we simulated a hardware-realistic artificial neural network (ANN) for MNIST handwritten digit classification. Figure 8 summarizes the network architecture, high-level circuit

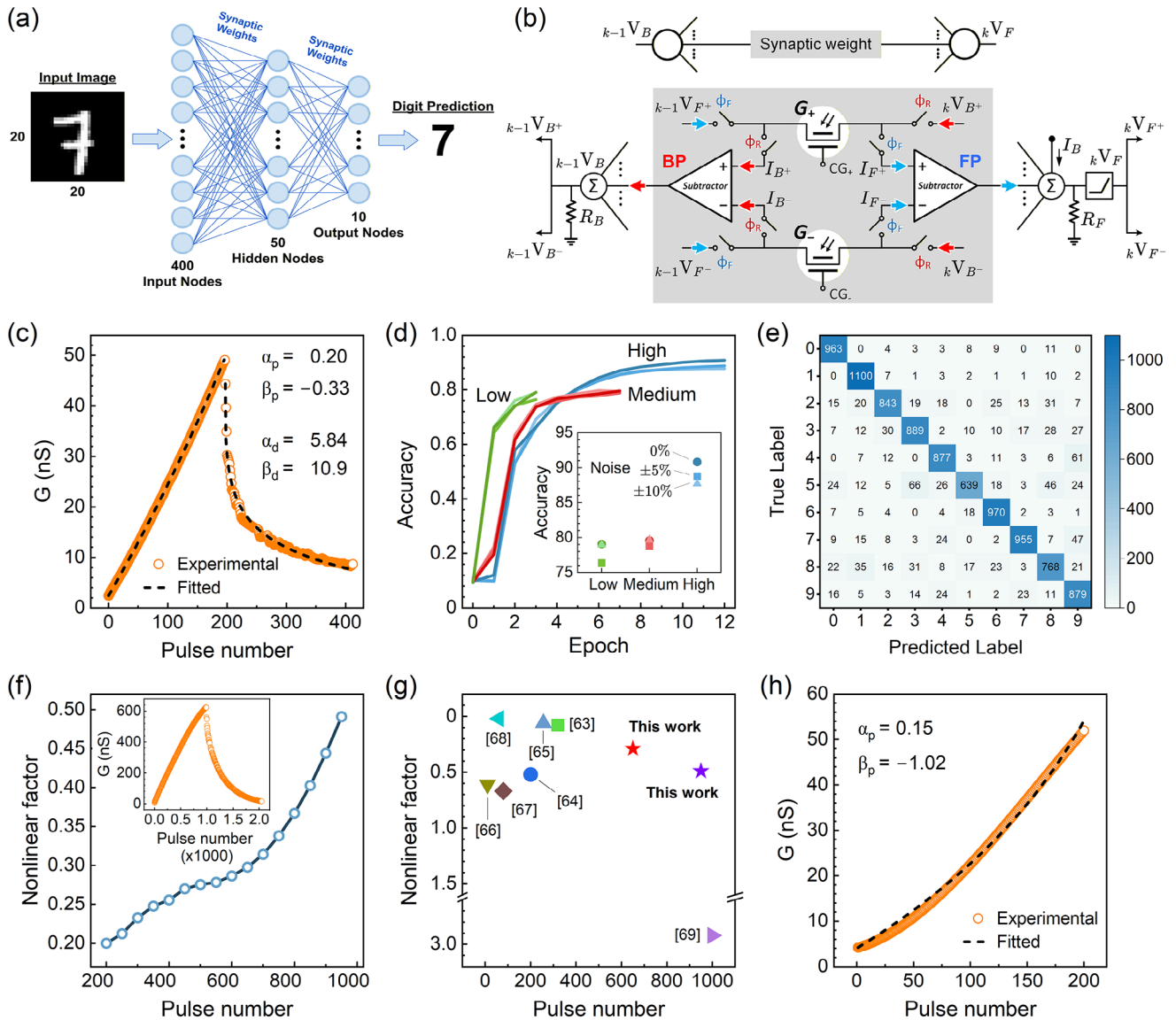

FIGURE 8 | Hardware artificial neural network (ANN) based on TIPS-Tc/IGZO synaptic phototransistors. (a) ANN schematic for MNIST handwritten-digit classification. (b) High-level circuit diagram of the differential synapse unit for weight updates, with switch-controlled enabling bidirectional current flow for error backpropagation. (c) Measured and modeled LTP–LTD conductance modulation under 535 nm illumination (5 μW·cm^{-2}, 0.25 s pulses), illustrating the conductance update protocol at medium resolution. (d) Classification accuracy under three weight-update resolution conditions, evaluated with noise levels of 0%, ±5%, and ±10%. (e) Confusion matrix for MNIST classification. (f) Nonlinearity (NL) factor versus cumulated pulse count; inset shows raw conductance traces used for NL extraction. (g) Comparison of NL factors and endurance with reported synaptic phototransistors [41, 65–70]. (h) LTP characteristics of the device operating in memory mode.

diagram, and training results. The ANN comprises two linear layers separated by a nonlinear activation (Figure 8a). The first layer maps 400 inputs to 50 outputs, followed by a LeakyReLU activation (leakage slope $\alpha = 0.1$), and the second layer maps 50 inputs to 10 output classes. Signed synaptic weights are implemented using differential (bipolar) encoding, where each weight is represented by a two-device differential synapse storing the positive conductance (G_+) and the negative (G_-) conductance component. The effective weight matrix during forward propagation is given by $W = G_+ - G_-$. Device-level weight updates follow previously reported protocols [64].

To emulate readout circuitry, each layer's output current was converted to a voltage input for the next layer through a 5 MΩ equivalent load. MNIST images (60 000 training and 10 000 test samples) were interpolated to 20 × 20 pixels (flattened to 400 inputs), and outputs were one-hot encoded (correct class at 5 V; others at 0 V). Training used stochastic gradient descent (SGD) with mean-squared error (MSE) loss. Backpropagation determined the update direction (sign), and the device conductance-change model (Equation 5) governed the update magnitude.

Each synapse unit (Figure 8b) comprises two identical TIPS-Tc/IGZO phototransistors contributing to the positive G_+ and negative G_- conductance components. A control-gate (CG) input enables long-term depression (LTD) for resetting or depressing the synaptic state as needed. The unit supports both forward

propagation (FP) and backward propagation (BP). During FP, the switch ϕ_F is closed and ϕ_R open, allowing the input voltage (V_F) to drive channel currents proportional to conductance. A differential subtractor then computes the synaptic output current $I_{out} = V_F (G_+ - G_-)$. During BP, the switches are reversed (ϕ_F open, ϕ_R closed) to enable error backpropagation that modulates device states. At each neuron, synaptic currents combine with a bias current (I_b) and drop across a forward resistor (R_F) to generate the neuron voltage, which is processed by the nonlinear activation and passed to the next layer.

Synaptic weights are updated optically, where each optical pulse incrementally increases or decreases conductance, and the step size defines learning resolution. Three conditions with varying pulse widths and/or wavelengths were tested to evaluate the trade-off between convergence and accuracy: (i) low resolution using 535 nm, 1 s pulses (Figure S15a); (ii) medium resolution (535 nm, 0.25 s pulses; Figure 8c); and (iii) high resolution using low-absorption 555 nm, 0.25 s pulses (Figure S15b). Higher resolution yielded higher final accuracy but slower convergence, whereas lower resolution enabled faster training with a slight loss in accuracy (Figure 8d). The MNIST test performance is summarized in the confusion matrix (Figure 8e).

To evaluate robustness under practical hardware conditions, noise was incorporated into the ANN simulations by introducing random perturbations in the synaptic update parameters (α and β) at levels of ±5% and ±10%. The network achieves >90% classification accuracy under the high-resolution setting (0% noise) and maintains stable performance across all resolution conditions, with accuracy remaining above ~87% even at ±10% noise, corresponding to only ~2%–3% degradation. This behavior is consistent with the relatively low nonlinearity (NL ≈ 0.2–0.5), which supports more uniform conductance updates and helps limit error accumulation during repeated programming. These results suggest that the proposed synaptic implementation can tolerate moderate noise levels without requiring explicit compensation in the present simulations, although additional optimization strategies could be applied if needed for further accuracy improvement.

The device's potentiation and depression dynamics are modeled by a compact conductance-update equation:

$$\begin{cases} G_p(n+1) = G_p(n) + \alpha_p e^{-\beta_p \frac{G_p(n)-G_{\min}}{G_{\max}-G_{\min}}} & 0 \le n \le 196 \\ G_d(n+1) = G_d(n) - \alpha_d e^{-\beta_d \frac{G_{\max}-G_d(n)}{G_{\max}-G_{\min}}} & 1 \le n \le 416 \end{cases} \quad (5)$$

Here, α_p and α_d define the initial step sizes, while β_p and β_d describe the nonlinearity of potentiation and depression, respectively (smaller β indicates a more linear update). $G_p(n)$ and $G_d(n)$ denote the conductance states during potentiation and depression after n optical pulses. Fitted parameters for the medium-resolution case are shown in the inset of Figure 8c. Note that a negative nonlinearity (NL) factor (β_p) occasionally arises when potentiation follows LTD due to residual hole diffusion that adds to the subsequent LTP current, producing an apparent overshoot. After each mini-batch (128 samples), a refresh operation re-centers saturated synapses by shifting both G_+ and G_- toward their mid-range values while preserving their differential weight ($G_+ - G_-$). A final clipping step enforces $G_{min} \le G \le G_{max}$.

Figure 8f shows the evolution of the cumulated NL factor, and its raw conductance traces (inset) under 985 potentiation pulses (535 nm, 10 μW·cm^{-2}, 0.25 s pulses, 0.5 s period). The device maintains low NL (<0.3) up to ~600 pulses, gradually increasing to ~0.49 at 950 pulses, reflecting an extended quasi-linear regime attributed to abundant trap sites in TIPS-Tc, slow hole detrapping, and low optical intensity per update. Figure 8g compares the NL factor and endurance with previously reported synaptic phototransistors, using normalized pulse count (pulse number × pulse width (s))/0.25 for direct comparison.

Figure 8h demonstrates long-term potentiation (LTP) in the memory mode, achieved by applying negative gate pulses to extend conductance retention (see Figure S16 for raw data). This dual-mode functionality enables fine-grained analog updates during training and stable retention during inference. It supports on-chip learning, power-gated inference, and simplified system design by integrating sensing, memory, and computation within a single device layer.

The combination of differential (bipolar) encoding and wavelength/pulse-programmable resolution provides stable, near-linear weight updates over hundreds of cycles and competitive MNIST classification accuracy under hardware-faithful training. The same device operated in memory mode ensures robust post-training retention, unifying training and inference in a compact, energy-efficient neuromorphic platform.

2.6 | Comparison With Mainstream Inorganic Photosynaptic Devices

To benchmark the performance of the proposed hybrid synaptic phototransistor, key figures of merit are summarized in Table 2, including update speed, weight-update linearity, electrical operating conditions, optical stimulus (wavelength and power density), and control functionality. These metrics enable direct comparison with representative mainstream inorganic photosynaptic devices based on oxide and 2D materials.

As shown in Table 2, many inorganic photosynaptic devices rely on UV or near-UV illumination (e.g., 255–365 nm for black phosphorus (BP) [71], and SnSe [72], and 350–365 nm for a-SIZO [73], and A-OSS systems [74],) and typically require mW·cm^{-2}-level optical power densities to induce persistent conductance changes. Even for devices operating at visible wavelengths, the required optical power generally ranges from hundreds of μW·cm^{-2} to tens of mW·cm^{-2}. In contrast, the TIPS-Tc/IGZO hybrid phototransistor operates under visible illumination (535 nm) with reliable responses down to ~0.5 μW·cm^{-2} in the weak-light regime and ~5 μW·cm^{-2} for LTP operation. This represents a substantial reduction in optical stimulus and directly lowers the energy per synaptic update, which is critical for large-scale neuromorphic systems.

This low optical operating power arises from the organic–inorganic hybrid architecture. The TIPS-Tc layer provides strong visible-light absorption, while interfacial charge transfer

TABLE 2 | Comparison of this work with representative mainstream inorganic optoelectronic synaptic devices.

Device/System	Speed (Optical pulse)	Linearity in LTP (NL)	Electrical conditions	Optical conditions	Control & Functionality	Refs.
TIPS-Tc/IGZO hybrid phototransistor	0.25–1 s	0.2–0.5	LTP: $V_g = -0.5$ V Erase: +10 (pulsed) Memory: −10 (pulsed) $V_{ds} = 1$ V	535 nm 0.5 μWcm^{-2} (weak) 5 μWcm^{-2} (LTP)	Gate-tunable multimode (LTP, LTD, erase, memory); 4 × 4 array	This work
α-In_2Se_3/Al_2O_3 phototransistor	1 s	0.52	LTP: $V_g = -10$ V LTD: +10 V $V_{ds} = 0.1$ V	450, 520, 675 nm 20 μWcm^{-2} (LTP)	Optical + electrical LTP/LTD (vision)	[65]
Black phosphorus phototransistor	1–300 ms	0.8–7	$V_{gs} = 0$ V $V_{ds} = 50$ mV	LTP: 280 nm, 3 mWcm^{-2} LTD: 365 nm, 6.8 mWcm^{-2}	All-optical memory + synapse; 2 × 2 array	[71]
SnSe thin-film synapse (2T)	1 s	2.72	2T; $V_{read} = 25$ mV	LTP: 430 nm, 5.1 mWcm^{-2} LTD: 255 nm, 122.5 μWcm^{-2}	All-optical bidirectional synapse	[72]
a-ZnAlSnO/SnO heterojunction (2T)	0.2–0.3 s	—	2T; $V_{read} = 0.1$ V	LTP: 635 nm, 15.28 μWcm^{-2} LTD: 532 nm, 32.8 μWcm^{-2} Reset: 405 nm	All-optical synapse (multi-wavelength)	[75]
A-OSS (ionogel-gated FET)	0.5 s	0.94 – 1.92	$V_{gs} = 0$ V $V_{ds} = 0.7$ V	365 nm, 1.3 mWcm^{-2}	Photo-synapse + electrical modulation	[74]
a-SIZO photo-TFT	3 s	—	$V_{gs} = -10$ V $V_{ds} = 5$ V	350 nm, -	STP/LTP photo-synapse	[73]
a-IGZO/ZrO_x phototransistor	0.5 s	—	$V_{gs} = 0$, 4 V $V_{ds} = 2$ V	LTP: 405 nm, 0.87 mWcm^{-2} LTD: 890 nm, 620 mWcm^{-2}	All-optical synapse	[76]
IGZO/SnO/SnS phototransistor	0.5 s	1.72	$V_{ds} = 2$ V	LTP: 266 nm, 0.82 mWcm^{-2} LTD: 658 nm, 2.94 mWcm^{-2}	All-optical synapse + memory; 8 × 8 array	[77]
Graphene/h-BN/ $MoTe_2$ /MoS_2 phototransistor	1 s	—	$V_{gs} = 5$ V $V_{ds} = 0.1$ V	LTP: 635 nm, 25.12 mWcm^{-2} Memory: 635 nm, 2.267 mWcm^{-2}	Photosensor + memory + synapse	[78]
InWZnO/WO_3 Phototransistor	0.5–2 s	0.089–0.102	$V_{gs} = -3$ V $V_{ds} = 0.1$ V	LTP: 460 nm, 525 nm, 650 nm, 0.254 mWcm^{-2}	Photo-synapse + memory	[79]

Abbreviations: 2T, two-terminal; A-OSS, artificial optical sensory synapse; a-SIZO, amorphous silicon–indium–zinc oxide; LTD, long-term depression; LTP, long-term potentiation;NL, nonlinearity factor; rGO, reduced graphene oxide; STP, short-term potentiation.

produces photogating amplification in the oxide channel, enabling synaptic modulation at low optical intensities. In addition, trap-mediated charge dynamics in the organic layer delay saturation during repeated stimulation, allowing gradual conductance modulation over extended pulse sequences.

Consistent with this mechanism, the device exhibits improved weight-update linearity, with a non-linearalrity (NL) factor of ~0.2–0.5 for LTP, lower than values reported for several inorganic photosynapses (e.g., α-In_2Se_3: 0.52; BP: ~0.8–7; SnSe: 2.72; IGZO/SnO/SnS: 1.72; A-OSS: 0.94–1.92), while some devices do not report NL explicitly. Lower nonlinearity enables more predictable incremental conductance updates, reducing cumulative programming errors and improving efficiency in analog weight training. The low NL factor arises from the large trap-density reservoir in the organic photoactive layer. Under low optical power, gradual trap filling delays saturation, enabling a near-linear LTP response over an extended period. In addition, the organic–inorganic architecture further separates the high-mobility conduction channel (inorganic) from the trap-rich layer (organic), preserving efficient charge transport while leveraging the high trap density required for linear transistor conductance modulation under optical stimulation.

Finally, field-controlled redistribution of trap charges in the photoactive organic layer enables gate-tunable multimode operation within a single device. By adjusting the gate-pulse scheme, the device can access LTP at subthreshold bias, LTD at positive V_g, and long-retention memory at negative V_g, while maintaining the same optical stimulus and device structure. This electrically programmable control simplifies system operation and is particularly advantageous for scalable neuromorphic arrays, where optical inputs are typically shared across many devices. In contrast, many inorganic photosynaptic devices rely on different

illumination wavelengths or two-terminal architectures where synaptic behavior is primarily governed by the optical stimulus or bias polarity, limiting flexible mode control. Combined with the demonstrated device array, this gate-programmable, low-power operation highlights the potential of the hybrid TIPS-Tc/IGZO photosynapse for energy-efficient and scalable neuromorphic hardware.

3 | Conclusion

We demonstrated a TIPS-Tc/IGZO hybrid synaptic phototransistor that integrates sensing, memory, and computation in a single, low-power platform. The type-II heterojunction facilitates electron transfer into IGZO while long-lived holes trapped in TIPS-Tc induce a persistent photogating effect, as confirmed by optical-electrical characterization and trap-dynamics modeling. Gate bias acts as an artificial neuromodulator, where negative pulses reinforce and stabilize conductance states (dopamine-like potentiation), while positive pulses accelerate relaxation and reset behavior (serotonin-like depression). This photoelectrically coupled control enables programmable transitions between learning and forgetting, emulating adaptive biological plasticity. The device operates under ultra-low visible illumination ($<5\ \mu W \cdot cm^{-2}$), enables weak-light imaging at $0.5\ \mu W \cdot cm^{-2}$, and exhibits retention exceeding 1000 s with high linearity suitable for array-level multiply-accumulate operations. System-level demonstrations highlight in-sensor capabilities, such as spatiotemporal trajectory capture and direction inference from current gradients, typically requiring separate sensing and memory modules. A device-calibrated ANN simulation using differential synapse pairs achieves >90% MNIST classification accuracy with near-linear weight updates across hundreds of steps, demonstrating seamless training and inference on the same hardware. Overall, these results establish the TIPS-Tc/IGZO hybrid as a biomimetic, energy-efficient optoelectronic synapse. Its neuromodulator-like gate control and persistent photocharge memory pave the way for compact, low-power neuromorphic vision and adaptive in-sensor computing at the edge.

4 | Experimental Section

4.1 | Device Fabrication

The device fabrication process followed our earlier report [80], with key steps summarized here. Bottom-gate IGZO TFTs were fabricated on heavily doped *p*-type Si substrates with a 300 nm SiO_2 dielectric. Substrates underwent standard solvent sonication, N_2 drying, and a brief prebake to remove moisture. A 25 nm thick IGZO active layer was deposited by RF magnetron sputtering from an In:Ga:Zn (1:1:1) target in an Ar/O_2 ambient using a shadow mask, followed by annealing at 400°C to activate the film. The oxygen partial pressure during deposition and post-annealing conditions was optimized to suppress dark current and improve detectivity; full parameters are detailed in ref. [80]. Thermally evaporated aluminum source and drain electrodes defined a channel geometry of 100 μm (L) × 1000 μm (W).

Before heterojunction formation, devices were subjected to a brief dehydration bake to minimize surface-adsorbed moisture, which can cause severe charge trapping and threshold voltage shifts in oxide TFTs. A toluene solution comprising 13.35 mM of the tetracene derivative 5,12-bis((triisopropylsilyl) ethynyl)tetracene (TIPS-Tc) and 5 $mg \cdot mL^{-1}$ of poly(methyl methacrylate) (PMMA) was prepared, yielding an average intermolecular distance of ~1 nm between TIPS-Tc molecules. The TIPS-Tc/PMMA blend was then spin-cast at 1500 rpm onto the IGZO TFTs, forming a 50 nm TIPS-Tc atop the IGZO channel. The stacked films were soft-baked in the dark at 85°C for 10 min to remove residual solvent. Except for characterization, all processing steps were carried out in a nitrogen glovebox. Any organic overcoat on the contact pads was carefully removed using an acetone-dampened swab.

4.2 | Optical and Electrical Characterization

Optical and electrical measurements were conducted under ambient conditions. Optical absorption was measured under illumination from a tungsten–halogen lamp focused onto the device using a 10 × objective to produce a near-diffraction-limited spot (<5 μm). The reflected signal was collected and analyzed using a SpectraPro HRS-300 spectrograph. Photoluminescence (PL) was excited at 450 nm using 100-–180 fs pulses at 10 kHz, generated via second-harmonic conversion (APE HarmoniXX) of femtosecond pulses from an optical parametric amplifier (ORPHEUS-F, Light Conversion). The excitation beam was focused onto the sample through the same optical path as in the absorption measurements, and PL emission was collected with a 500 nm long-pass filter to block the excitation light.

Photoluminescence (PL) lifetime measurements were conducted using time-correlated single-photon counting (TCSPC) with 532 nm picosecond pulsed excitation from a frequency-doubled Nd:YAG laser (HE-1060, 500 kHz repetition rate). The emitted light was passed through a 532 nm long-pass filter and detected by a single-photon avalanche photodiode (SPAD; Molecular Photonic Devices) coupled to a TCSPC module (TimeHarp 200, PicoQuant Inc.). The instrument response function exhibited a temporal resolution of approximately 380 ps.

Current–voltage (I–V) characteristics were measured using a Keithley 2636B source-measure unit with a custom probing adapter. Wavelength-selective excitation from a Horiba FluoroMax-4 fluorospectrometer was coupled to the sample and focused by a 4 × objective. A neutral-density filter was used to maintain constant power density across wavelengths. Time-resolved photocurrent responses were recorded with a Keithley 2400 sourcemeter. All measurements were performed under controlled ambient conditions, and device performance was verified to be stable under moderate humidity variations (see Figure S17 in Supporting Information).

Acknowledgements

The authors thank Prof. J. Anthony for the TIPS-Tc derivatives and Rick Presley and Chris Tasker for their assistance with the RF sputtering

and thermal evaporation tools. This work was supported in part by the National Science Foundation (NSF) (CHE-1956431 to O.O). Part of this research was conducted at the Northwest Nanotechnology Infrastructure, a National Nanotechnology Coordinated Infrastructure (NNCI) site at Oregon State University, supported in part by NSF grant NNCI-2025489 and Oregon State University.

Conflicts of Interest

The authors declare no conflicts of interest.

Data Availability Statement

The data supporting the findings of this study are available in the Supporting Information of this article.

References

1. Y.-J. Du, J. Yang, Z. Lv, et al., "Integration of Perovskite/Low-Dimensional Material Heterostructures for Optoelectronics and Artificial Visual Systems," *Advanced Functional Materials* 35 (2025): 2500953, https://doi.org/10.1002/adfm.202500953.

2. J. Zhang, J. Liu, H. Geng, et al., "Low Power Consumption $CsPb_{0.5}Sn_{0.5}Br_3$ Quantum Dot-Based Photoelectric Synaptic Transistors for Neuromorphic Computing," *ACS Applied Nano Mater* 8 (2025): 13573.

3. S. Kumar, X. Wang, J. P. Strachan, Y. Yang, and W. D. Lu, "Dynamical Memristors for Higher-Complexity Neuromorphic Computing," *Nature Reviews Materials* 7 (2022): 575–591, https://doi.org/10.1038/s41578-022-00434-z.

4. Y.-C. Lin, W.-C. Yang, Y.-C. Chiang, and W.-C. Chen, "Recent Advances in Organic Phototransistors: Nonvolatile Memory, Artificial Synapses, and Photodetectors," *Small Science* 2 (2022): 2100109.

5. S. Lee, Y. K. Kim, J. Noh, B. C. Jang, and S. Lee, "More-Than-Moore Approaches Implemented Using van der Waals Heterostructures," *ACS Nano* 19 (2025): 29028–29048, https://doi.org/10.1021/acsnano.5c07260.

6. B. Tossoun, D. Liang, S. Cheung, et al., "High-Speed and Energy-efficient Non-volatile Silicon Photonic Memory Based on Heterogeneously Integrated Memresonator," *Nature Communications* 15 (2024): 551, https://doi.org/10.1038/s41467-024-44773-7.

7. D. Marković, A. Mizrahi, D. Querlioz, and J. Grollier, "Physics for Neuromorphic Computing," *Nature Reviews Physics* 2 (2020): 499–510, https://doi.org/10.1038/s42254-020-0208-2.

8. L. Yu and Y. Yu, "Energy-Efficient Neural Information Processing in Individual Neurons and Neuronal Networks," *Journal of Neuroscience Research* 95 (2017): 2253–2266, https://doi.org/10.1002/jnr.24131.

9. K.-U. Demasius, A. Kirschen, and S. Parkin, "Energy-Efficient Memcapacitor Devices for Neuromorphic Computing," *Nature Electronics* 4 (2021): 748–756, https://doi.org/10.1038/s41928-021-00649-y.

10. D. Liu, H. Yu, and Y. Chai, "Low-Power Computing with Neuromorphic Engineering," *Advanced Intelligent Systems* 3 (2021): 2000150, https://doi.org/10.1002/aisy.202000150.

11. F. Nadim and D. Bucher, "Neuromodulation of Neurons and Synapses," *Current Opinion in Neurobiology* 29 (2014): 48–56, https://doi.org/10.1016/j.conb.2014.05.003.

12. K. Z. Peters, J. F. Cheer, and R. Tonini, "Modulating the Neuromodulators: Dopamine, Serotonin, and the Endocannabinoid System," *Trends in Neurosciences* 44 (2021): 464–477, https://doi.org/10.1016/j.tins.2021.02.001.

13. Q. Gu, "Neuromodulatory Transmitter Systems in the Cortex and Their Role in Cortical Plasticity," *Neuroscience* 111 (2002): 815–835, https://doi.org/10.1016/S0306-4522(02)00026-X.

14. E. E. Steinberg, R. Keiflin, J. R. Boivin, I. B. Witten, K. Deisseroth, and P. H. Janak, "A Causal Link Between Prediction Errors, Dopamine Neurons and Learning," *Nature Neuroscience* 16 (2013): 966–973, https://doi.org/10.1038/nn.3413.

15. W. Schultz, "Getting Formal with Dopamine and Reward," *Neuron* 36 (2002): 241–263, https://doi.org/10.1016/S0896-6273(02)00967-4.

16. H. Liu, T. Wu, X. G. Canales, et al., "Forgetting Generates a Novel state That Is Reactivatable," *Science Advances* 8 (2022): abi9071, https://doi.org/10.1126/sciadv.abi9071.

17. X. Huang, M. Wang, W. Wen, et al., "Constructing Perovskite Organic Phototransistors Using a Triple Strategy to Achieve Visible and NIR Visual Synapses and Adaptive Functions," *Small* 21 (2025): 2412025, https://doi.org/10.1002/smll.202412025.

18. F. Zhou and Y. Chai, "Near-Sensor and in-Sensor Computing," *Nature Electronics* 3 (2020): 664–671, https://doi.org/10.1038/s41928-020-00501-9.

19. Z. Cheng, C. Ríos, W. H. Pernice, C. D. Wright, and H. Bhaskaran, "On-Chip Photonic Synapse," *Science advances* 3 (2017): 1700160.

20. H. Hendy and C. Merkel, "Review of Spike-Based Neuromorphic Computing for Brain-Inspired Vision: Biology, Algorithms, and Hardware," *Journal of Electronic Imaging* 31 (2022): 010901.

21. X. Yang, J. Yan, W. Wang, S. Li, B. Hu, and J. Lin, "Brain-Inspired Models for Visual Object Recognition: An Overview," *Artificial Intelligence Review* 55 (2022): 5263–5311, https://doi.org/10.1007/s10462-021-10130-z.

22. Z. Guo, J. Zhang, X. Liu, L. Wang, L. Xiong, and J. Huang, "Optoelectronic Synapses and Photodetectors Based on Organic Semiconductor/Halide Perovskite Heterojunctions: Materials, Devices, and Applications," *Advanced Functional Materials* 33 (2023): 2305508, https://doi.org/10.1002/adfm.202305508.

23. Q. Zhang, T. Jin, X. Ye, D. Geng, W. Chen, and W. Hu, "Organic Field Effect Transistor-Based Photonic Synapses: Materials, Devices, and Applications," *Advanced Functional Materials* 31 (2021): 2106151, https://doi.org/10.1002/adfm.202106151.

24. M. Sawatzki-Park, S.-J. Wang, H. Kleemann, and K. Leo, "Highly Ordered Small Molecule Organic Semiconductor Thin-Films Enabling Complex, High-Performance Multi-Junction Devices," *Chemical Reviews* 123 (2023): 8232–8250, https://doi.org/10.1021/acs.chemrev.2c00844.

25. A.-C. Chang, Y.-C. Lin, H.-C. Yen, W.-C. Yang, Y.-F. Yang, and W.-C. Chen, "Unraveling the Singlet Fission Effects on Charge Modulations of Organic Phototransistor Memory Devices," *ACS Applied Electronic Materials* 4 (2022): 1266–1276, https://doi.org/10.1021/acsaelm.1c01345.

26. Y.-S. Wu, A.-C. Chang, W.-C. Chen, et al., "High-Performance Synaptic Phototransistor Using a Photoactive Self-Assembled Layer toward Ultralow Energy Consumption," *Advanced Optical Materials* 12 (2024): 2302040, https://doi.org/10.1002/adom.202302040.

27. Y. Lee, H.-L. Park, Y. Kim, and T.-W. Lee, "Organic Electronic Synapses with Low Energy Consumption," *Joule* 5 (2021): 794–810, https://doi.org/10.1016/j.joule.2021.01.005.

28. N. Sui, Y. Ji, M. Li, et al., "Photoprogrammed Multifunctional Optoelectronic Synaptic Transistor Arrays Based on Photosensitive Polymer-Sorted Semiconducting Single-Walled Carbon Nanotubes for Image Recognition," *Advanced Science* 11 (2024): 2401794, https://doi.org/10.1002/advs.202401794.

29. J. Kim, S.-M. Kwon, Y. K. Kang, et al., "A Skin-Like Two-Dimensionally Pixelized Full-Color Quantum Dot Photodetector," *Science Advances* 5 (2019): aax8801, https://doi.org/10.1126/sciadv.aax8801.

30. W. Liu, W. Chen, C. Jin, et al., "Organic Optoelectrical Synaptic Transistors for Color Information Processing," *Applied Physics Letters* 123 (2023): 193703, https://doi.org/10.1063/5.0173413.

31. J. Zhang, S. Dai, Y. Zhao, J. Zhang, and J. Huang, "Recent Progress in Photonic Synapses for Neuromorphic Systems," *Advanced Intelligent Systems* 2 (2020): 1900136, https://doi.org/10.1002/aisy.201900136.

32. M. Li, C. Li, K. Ye, et al., "Self-Powered Photonic Synapses with Rapid Optical Erasing Ability for Neuromorphic Visual Perception," *Research* 7 (2024): 0526, https://doi.org/10.34133/research.0526.

33. J. Wu, X. Wang, X. Tang, et al., "Low-Power and Multimodal Organic Photoelectric Synaptic Transistors Modulated by Photoisomerization for

UV Damage Perception and Artificial Visual Recognition," *Advanced Functional Materials* 35 (2025): 2420073, https://doi.org/10.1002/adfm.202420073.

34. W. T. Goldthwaite, E. Lambertson, M. Gragg, et al., "Morphology- and Crystal Packing-Dependent Singlet Fission and Photodegradation in Functionalized Tetracene Crystals and Films," *The Journal of Chemical Physics* 161 (2024): 194712, https://doi.org/10.1063/5.0234494.

35. Y. Wan, Z. Guo, T. Zhu, S. Yan, J. Johnson, and L. Huang, "Cooperative Singlet and Triplet Exciton Transport in Tetracene Crystals Visualized by Ultrafast Microscopy," *Nature Chemistry* 7 (2015): 785–792, https://doi.org/10.1038/nchem.2348.

36. R. W. I. de Boer, M. Jochemsen, T. M. Klapwijk, et al., "Space Charge Limited Transport and Time of Flight Measurements in Tetracene Single Crystals: a Comparative Study," *Journal of Applied Physics* 95 (2004): 1196–1202, https://doi.org/10.1063/1.1631079.

37. C. Liu, C. Gao, W. Huang, et al., "Bipolar Synaptic Organic/Inorganic Heterojunction Transistor with Complementary Light Modulation and Low Power Consumption for Energy-Efficient Artificial Vision Systems," *Science China Materials* 67 (2024): 1500–1508, https://doi.org/10.1007/s40843-024-2812-7.

38. L. Zhu, S. Li, J. Lin, et al., "Ultra-Low Power IGZO Optoelectronic Synaptic Transistors for Neuromorphic Computing," *Science China Information Sciences* 67 (2024): 222401, https://doi.org/10.1007/s11432-023-3966-8.

39. X. Wu, S. Shi, B. Liang, et al., "Ultralow-power Optoelectronic Synaptic Transistors Based on Polyzwitterion Dielectrics for in-sensor Reservoir Computing," *Science Advances* 10 (2024): adn4524, https://doi.org/10.1126/sciadv.adn4524.

40. X. Han, J. Tao, Y. Liang, et al., "Ultraweak Light-Modulated Heterostructure with Bidirectional Photoresponse for Static and Dynamic Image Perception," *Nature Communications* 15 (2024): 10430, https://doi.org/10.1038/s41467-024-54845-3.

41. P. Guo, J. Zhang, Z. Hua, et al., "Organic Synaptic Transistors Based on a Semiconductor Heterojunction for Artificial Visual and Neuromorphic Functions," *Nano Letters* 25 (2025): 3204–3211, https://doi.org/10.1021/acs.nanolett.4c05809.

42. Z. Guo, J. Zhang, B. Yang, et al., "Organic High-Temperature Synaptic Phototransistors for Energy-Efficient Neuromorphic Computing," *Advanced Materials* 36 (2024): 2310155, https://doi.org/10.1002/adma.202310155.

43. Z. Liang, X. Wang, Z. Song, et al., "Organic Optoelectronic Synaptic Transistor with Enhanced UV Light Response Based on Insulating Polymer-Assisted p–n Heterojunction," *ACS Applied Materials & Interfaces* 16 (2024): 65091–65099, https://doi.org/10.1021/acsami.4c12583.

44. K. Paudel, B. Johnson, A. Neunzert, et al., "Small-Molecule Bulk Heterojunctions: Distinguishing Between Effects of Energy Offsets and Molecular Packing on Optoelectronic Properties," *The Journal of Physical Chemistry C* 117 (2013): 24752–24760, https://doi.org/10.1021/jp4093089.

45. K. Paudel, G. Giesbers, J. Van Schenck, J. E. Anthony, and O. Ostroverkhova, "Molecular Packing-Dependent Photoconductivity in Functionalized Anthradithiophene Crystals," *Organic Electronics* 67 (2019): 311–319, https://doi.org/10.1016/j.orgel.2018.12.040.

46. A. Ortiz-Conde, F. J. Garcıá Sánchez, J. J. Liou, A. Cerdeira, M. Estrada, and Y. Yue, "A Review of Recent MOSFET Threshold Voltage Extraction Methods," *Microelectronics Reliability* 42 (2002): 583–596, https://doi.org/10.1016/S0026-2714(02)00027-6.

47. F. Ventriglia and V. Di Maio, "Stochastic Fluctuations of the Quantal EPSC Amplitude in Computer Simulated Excitatory Synapses of Hippocampus," *Bio Systems* 71 (2003): 195–204, https://doi.org/10.1016/S0303-2647(03)00117-5.

48. W. Wang, S. Li, Y. Tanaka, and T. Takada, "Interfacial Charge Dynamics of Cross-Linked Polyethylene/Ethylene-Propylene-Diene Dual Dielectric Polymer as Revealed by Energy Band Structure," *IEEE Transactions on Dielectrics and Electrical Insulation* 26 (2019): 1755–1762, https://doi.org/10.1109/TDEI.2019.008122.

49. F. Rogti and M. Ferhat, "Effect of Temperature on Trap Depth Formation in Multi-Layer Insulation: Low Density Polyethylene and Fluorinated Ethylene Propylene," *Applied Physics Letters* 104 (2014): 031605, https://doi.org/10.1063/1.4862061.

50. M. Taleb, G. Teyssedre, S. L. Roy, and C. Laurent, "Modeling of Charge Injection and Extraction in a Metal/Polymer Interface Through an Exponential Distribution of Surface States," *IEEE Transactions on Dielectrics and Electrical Insulation* 20 (2013): 311–320, https://doi.org/10.1109/TDEI.2013.6451372.

51. A. Abate, D. R. Staff, D. J. Hollman, H. J. Snaith, and A. B. Walker, "Influence of Ionizing Dopants on Charge Transport in Organic Semiconductors," *Physical Chemistry Chemical Physics* 16 (2014): 1132–1138, https://doi.org/10.1039/C3CP53834F.

52. A. Ullah, R. Lamug, X. Zhang, O. Ostroverkhova, and L.-J. Cheng, "Trap-Mediated Photogating in Hybrid Organic–Inorganic Heterojunction Phototransistors for Photo-Memory and Photodetection," *Journal of Materials Chemistry C* 14 (2026): 7150–7160.

53. L. Kulikovsky, D. Neher, E. Mecher, K. Meerholz, H.-H. Hörhold, and O. Ostroverkhova, "Photocurrent Dynamics in a Poly(phenylene vinylene)-Based Photorefractive Composite," *Physical Review B* 69 (2004): 125216, https://doi.org/10.1103/PhysRevB.69.125216.

54. O. Ostroverkhova and W. E. Moerner, "Organic Photorefractives: Mechanisms, Materials, and Applications," *Chemical Reviews* 104 (2004): 3267–3314, https://doi.org/10.1021/cr960055c.

55. O. Ostroverkhova and K. D. Singer, "Space-Charge Dynamics in Photorefractive Polymers," *Journal of Applied Physics* 92 (2002): 1727–1743, https://doi.org/10.1063/1.1491279.

56. Y. Sun, L. Zhang, Z. Ahmed, and M. Chan, "Characterization of Interface Trap Dynamics Responsible for Hysteresis in Organic Thin-Film Transistors," *Organic Electronics* 27 (2015): 192–196, https://doi.org/10.1016/j.orgel.2015.09.011.

57. K. Lee, M. S. Oh, S. Mun, et al., "Interfacial Trap Density-of-States in Pentacene- and ZnO-Based Thin-Film Transistors Measured via Novel Photo-Excited Charge-Collection Spectroscopy," *Advanced Materials* 22 (2010): 3260–3265, https://doi.org/10.1002/adma.201000722.

58. S. Anand, K. P. Goetz, Z. A. Lamport, A. M. Zeidell, and O. D. Jurchescu, "Field-Dependent Charge Transport in Organic Thin-Film Transistors: Impact of Device Structure and Organic Semiconductor Microstructure," *Applied Physics Letters* 115 (2019): 073301, https://doi.org/10.1063/1.5099388.

59. O. Ostroverkhova, "Organic Optoelectronic Materials: Mechanisms and Applications," *Chemical Reviews* 116 (2016): 13279–13412, https://doi.org/10.1021/acs.chemrev.6b00127.

60. S. Kim, H. Yoo, and J. Choi, "Effects of Charge Traps on Hysteresis in Organic Field-Effect Transistors and Their Charge Trap Cause Analysis through Causal Inference Techniques," *Sensors* 23 (2023): 2265, https://doi.org/10.3390/s23042265.

61. A. Di Bartolomeo, L. Genovese, T. Foller, et al., "Electrical Transport and Persistent Photoconductivity in Monolayer MoS_2 Phototransistors," *Nanotechnology* 28 (2017): 214002, https://doi.org/10.1088/1361-6528/aa6d98.

62. O. Liba, K. Murthy, Y.-T. Tsai, et al., "Handheld Mobile Photography in Very Low Light," *ACM Transactions on Graphics* 38 (2019): 1–16, https://doi.org/10.1145/3355089.3356508.

63. S. W. Hasinoff, D. Sharlet, R. Geiss, et al., "Burst Photography for High Dynamic Range and Low-Light Imaging on Mobile Cameras," *ACM Transactions on Graphics* 35 (2016): 192.

64. S. Lim, J.-H. Bae, J.-H. Eum, et al., "Adaptive Learning Rule for Hardware-Based Deep Neural Networks Using Electronic Synapse Devices," *Neural Computing and Applications* 31 (2019): 8101–8116, https://doi.org/10.1007/s00521-018-3659-y.

65. Y. Chen, M. Zhang, D. Li, et al., "Bidirectional Synaptic Phototransistor Based on Two-Dimensional Ferroelectric Semiconductor for Mixed Color Pattern Recognition," *ACS Nano* 17 (2023): 12499–12509, https://doi.org/10.1021/acsnano.3c02167.

66. J. Park, J. O. Kim, and S.-W. Kang, "Lateral Heterostructures of WS_2 and MoS_2 Monolayers for Photo-Synaptic Transistor," *Scientific Reports* 14 (2024): 6922, https://doi.org/10.1038/s41598-024-57642-6.

67. R. Martinez-Martinez, M. M. Islam, A. Krishnaprasad, and T. Roy, "Graphene–Oxide Interface for Optoelectronic Synapse Application," *Scientific Reports* 12 (2022): 5880, https://doi.org/10.1038/s41598-022-09873-8.

68. X. Wang, S. Yang, Z. Qin, B. Hu, L. Bu, and G. Lu, "Enhanced Multiwavelength Response of Flexible Synaptic Transistors for Human Sunburned Skin Simulation and Neuromorphic Computation," *Advanced Materials* 35 (2023): 2303699, https://doi.org/10.1002/adma.202303699.

69. D. Li, R. Hu, Y. Zhu, et al., "Boosting the Charge Injection of Polymer Electrets for Light-Stimulated Artificial Synaptic Transistors," *Journal of Materials Chemistry C* 12 (2024): 13797–13808, https://doi.org/10.1039/D4TC02706J.

70. M. M. Islam, D. Dev, A. Krishnaprasad, L. Tetard, and T. Roy, "Optoelectronic Synapse Using Monolayer MoS_2 Field Effect Transistors," *Scientific Reports* 10 (2020): 21870, https://doi.org/10.1038/s41598-020-78767-4.

71. T. Ahmed, M. Tahir, M. X. Low, et al., "Fully Light-Controlled Memory and Neuromorphic Computation in Layered Black Phosphorus," *Advanced Materials* 33 (2021): 2004207, https://doi.org/10.1002/adma.202004207.

72. H. Chen, D. Huang, Z. Zhang, S. Wang, Y. Han, and H. Huang, "All-Optical Modulated Bidirectional Responsive Synaptic Devices: Materials, Mechanisms, and Applications," *Advanced Optical Materials* 14 (2026): 03737, https://doi.org/10.1002/adom.202503737.

73. A. Sarkar and S. Y. Lee, "Efficient UV-Sensitive Si-In-ZnO-Based Photo-TFT and Its Behavior as an Optically Stimulated Artificial Synapse," *ACS Applied Electronic Materials* 5 (2023): 1057–1066, https://doi.org/10.1021/acsaelm.2c01559.

74. A. Bag, J. W. Lee, Y. R. Lee, and N.-E. Lee, "A Flexible Artificial Optical Synapse with Photo-Gating Based on a Heterojunction Channel of Reduced Graphene Oxide and ZnO Nanorods," *Advanced Functional Materials* 36 (2026): 18534, https://doi.org/10.1002/adfm.202518534.

75. R. Yang, Y. Wang, S. Li, et al., "All-Optically Controlled Artificial Synapse Based on Full Oxides for Low-Power Visible Neural Network Computing," *Advanced Functional Materials* 34 (2024): 2312444, https://doi.org/10.1002/adfm.202312444.

76. Y.-C. Mi, C.-H. Yang, L.-C. Shih, and J.-S. Chen, "All-Optical-Controlled Excitatory and Inhibitory Synaptic Signaling Through Bipolar Photoresponse of an Oxide-Based Phototransistor," *Advanced Optical Materials* 11 (2023): 2300089, https://doi.org/10.1002/adom.202300089.

77. T. Zhang, C. Fan, L. Hu, F. Zhuge, X. Pan, and Z. Ye, "A Reconfigurable All-Optical-Controlled Synaptic Device for Neuromorphic Computing Applications," *ACS Nano* 18 (2024): 16236–16247, https://doi.org/10.1021/acsnano.4c02278.

78. T. Zhao, W. Yue, Q. Deng, et al., "Neuromorphic Transistors Integrating Photo-Sensor, Optical Memory and Visual Synapses for Artificial Vision Application," *Advanced Materials* 37 (2025): 2419208, https://doi.org/10.1002/adma.202419208.

79. J.-L. Chen, T.-C. Chiang, and P.-T. Liu, "All-Metal-Oxide Heterojunction Optoelectronic Synapses with Multilevel Memory for Artificial Visual Perception Applications," *Small* 21 (2025): 2502271, https://doi.org/10.1002/smll.202502271.

80. A. Ullah, R. Lamug, X. Zhang, O. Ostroverkhova, and L.-J. Cheng, "Highly Sensitive and Fast-Response Hybrid Phototransistors Enabled by Dynamic Photogating in Anthradithiophene-Metal Oxide Heterojunctions," *Advanced Optical Materials* 13 (2025): 2500081, https://doi.org/10.1002/adom.202500081.

Supporting Information

Additional supporting information can be found online in the Supporting Information section.

Supporting File 1: adfm75942-sup-0001-SuppMat.pdf.